Supplemental Information

Title: Benchmarking HER and OER Electrocatalysts for Solar Water Splitting Devices

Authors: Charles C. L. McCrory, Suho Jung, Ivonne M. Ferrer, Shawn M. Chatman, Jonas C. Peters, and Thomas F. Jaramillo

Section S1: Materials and Electrolysis Cell Design

Materials. Materials were purchased in the grade indicated and used as received. Ammonium carbonate ($(NH_4)_2CO_3$, 99.999%), ammonium chloride (NH_4Cl. BioUltra), ammonium hydroxide (NH_4OH, BioUltra), ammonium perchlorate (NH_4ClO_4, 99.999%), ammonium sulfate ($(NH_4)_2SO_4$, 99.999%), ammonium tetrathiomolybdate ($(NH_4)[MoS_4]$, 99.97%), boric acid (H_3BO_3, BioUltra), chromium(III) sulfate monohydrate ($Cr_2(SO_4)_3 \cdot H_2O$, 99.999%), cobalt(II) acetate tetrahydrate ($Co(OAc)_2 \cdot 4H_2O$, 99.999%), cobalt(II) chloride hexahydrate ($CoCl_2 \cdot 6H_2O$, ACS 98%), cobalt(II) nitrate hexahydrate ($Co(NO_3)_2 \cdot 6H_2O$, 99.999%), copper(II) sulfate heptahydrate ($CuSO_4 \cdot 5H_2O$, 99.995%), glycine (NH_2CH_2COOH, BioUltra), iridium(III) acetylacetonate ($Ir(acac)_3$, 97%), iron(II) chloride tetrahydrate ($FeCl_2 \cdot 4H_2O$, 99.99%), iron(III) chloride heptahydrate ($FeCl_3 \cdot 6H_2O$, ACS 97%), iron(III) nitrate nonahydrate ($Fe(NO_3)_3 \cdot 9H_2O$, 99.99%), iron(II) sulfate heptahydrate ($FeSO_4 \cdot 7H_2O$, ACS 99%), manganese(II) sulfate hydrate ($MnSO_4 \cdot H_2O$, 99.99%), nickel(II) nitrate hexahydrate ($Ni(NO_3)_2 \cdot 6\ H_2O$, 99.999%), nickel(II) sulfate hexahydrate ($NiSO_4 \cdot 6H_2O$, 99.99%),nickel(II) chloride hexahydrate ($NiCl_2 \cdot 6H_2O$, 99.9%), phosphotungstic acid hydrate ($H_3PW_{12}O_{40} \cdot nH_2O$, 99.995%), potassium citrate tribasic monohydrate ($K_3C_6H_5O_7 \cdot H_2O$, 99%), potassium hydroxide (KOH, BioXtra), potassium pyrophosphate ($K_4P_2O_7$, 97%), saccharin (99%), sodium acetate trihydrate ($NaOAc \cdot 3H_2O$, BioUltra), sodium bicarbonate ($NaHCO_3$, BioXtra), sodium carbonate (Na_2CO_3, BioUltra), sodium chloride (NaCl, BioUltra), sodium citrate tribasic dihydrate ($Na_3C_6H_5O_7 \cdot 2H_2O$, BioUltra), sodium dodecyl sulfate (SDS, BioUltra), sodium hydroxide (NaOH, BioUltra), sodium hypophosphite monohydrate ($NaH_2PO_2 \cdot H_2O$, 99%), sodium molybdate dihydrate ($Na_2MoO_4 \cdot 2H_2O$, 99.99%), sodium perchlorate monohydrate ($NaClO_4 \cdot H_2O$, ACS 98%), sodium pyrophosphate decahydrate ($Na_4P_2O_7 \cdot 10H_2O$, ACS 99%), sodium sulfate decahydrate ($Na_2SO_4 \cdot 10H_2O$, BioUltra), sodium tungstate dihydrate ($Na_2WO_4 \cdot 2H_2O$, BioUltra), tin(II) chloride dihydrate ($SnCl_2 \cdot 2H_2O$, 99.99%), and zinc sulfate heptahydrate ($ZnSO_4 \cdot 7H_2O$, 99.999%) were purchased from Sigma-Aldrich. REacton grade cerium(III) nitrate hexahydrate ($Ce(NO_3)_3 \cdot 6H_2O$, 99.99%) and lanthanum(III) nitrate hexahydrate ($La(NO_3)_3 \cdot 6H_2O$, 99.999%), and Puratronic grade cobalt(II) sulfate heptahydrate ($CoSO_4 \cdot 7\ H_2O$, 99.999%) and copper(II) nitrate hexahydrate ($Cu(NO_3)_2 \cdot 6H_2O$, 99.999%) were purchased from Alfa Aesar. TraceMetal grade 37% hydrochloric acid (HCl), and 98% sulfuric acid (H_2SO_4) were purchased from Fisher Scientific, and TraceSelect grade L-ascorbic acid (99.9998%), 69% nitric acid (HNO_3) and potassium phosphate monobasic (KH_2PO_4, 99.995%) were purchased from Sigma-Aldrich. Technical grade tetraethylpentamine (TEPA) was purchased from Strem Chemicals. ACS grade 2-propanol and acetone were purchased from VWR.

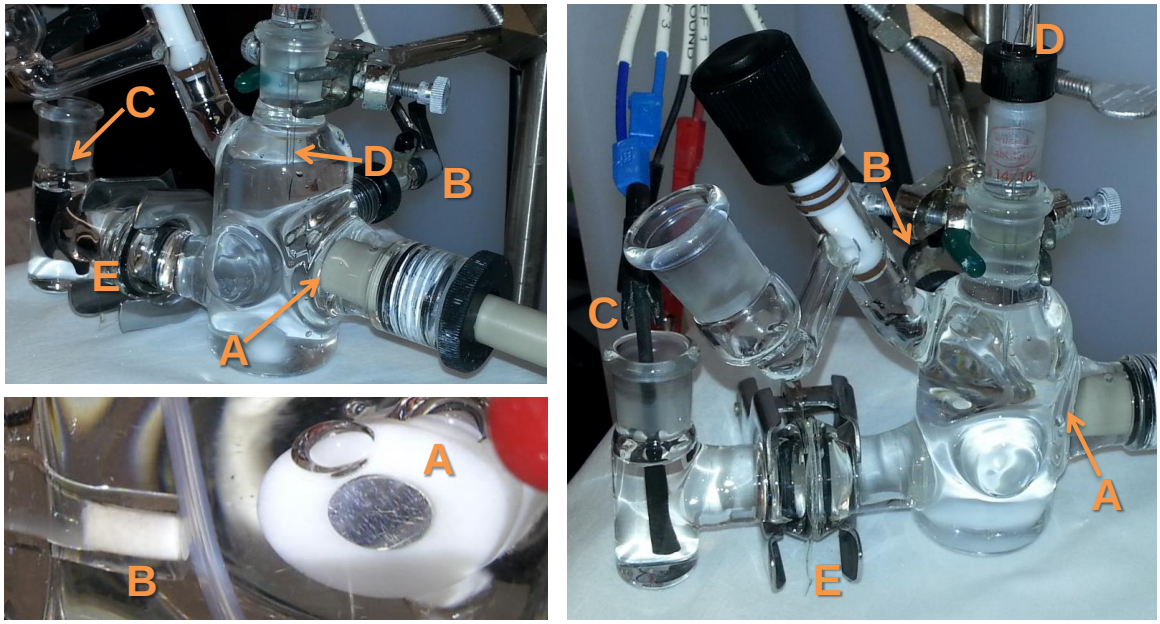

Figure S1. Photograph of custom two-compartment electrolysis cell: (A) Working electrode with compression fitting with Teflon holder, (B) sealed SCE reference electrode, (C) C auxiliary electrode, (D) Unisense Ox-500 or H_2-500 probe, and (E) 0.007 inch Nafion-117 membrane. In general, gas-tight seals were made either by o-ring compression or with ground-glass joints.

Section S2: Electrodeposition Conditions

Table S1. Electrodeposited HER Catalysts investigated along with deposition conditions

Catalyst	Deposition Solution (in 40 mL H_2O)	Deposition Conditions	Reference
Co-(a)	1 g $Co(OAc)_2 \cdot 4H_2O$, 1.2 g NaCl	Cathodic deposition at -5 mA cm^{-2} for 7200 s, 400 rpm	S1
CoMo [a]	3.36 g $CoSO_4 \cdot 7H_2O$, 1.92 $Na_2MoO_4 \cdot 2H_2O$, 3.52 $Na_3C_6H_5O_7 \cdot 2H_2O$, NH_4OH to pH 10.5[a]	Cathodic deposition at -100 mA cm^{-2} for 1200 s, 800 rpm	S2
CoNiFe	1.902 g $NiCl_2 \cdot 6H_2O$, 1.428 g $CoCl_2 \cdot 6H_2O$, 0.318 g $FeCl_2 \cdot 4H_2O$, 1.636 g NaCl, 0.989 g H_3BO_3, 0.055 g saccharin, 0.352 g L-ascorbic acid, pH 3	Cathodic deposition at -10 mA cm^{-2} for 1000 s, 400 rpm, under N_2	S3
CoW	6.8 g $CoSO_4 \cdot 7H_2O$, 0.4 $Na_2WO_4 \cdot 2H_2O$, 8 $Na_3C_6H_5O_7 \cdot 2H_2O$, 2 g NH_4Cl, pH 9.0	Cathodic deposition at -40 mA cm^{-2} for 1200 s, 1200 rpm, 70 °C	S2
Fe-(a)	12.01 g $FeSO_4 \cdot 7H_2O$, 0.241 g $FeCl_2 \cdot 4H_2O$, 0.113 g H_3BO_3, H_2SO_4 to pH 2.5	Cathodic deposition at -50 mA cm^{-2} for 680 s, 400 rpm	S4
FeMo	0.60 g $FeCl_3 \cdot 6H_2O$, 1.9 g $NaMoO_4 \cdot 2H_2O$, 3.0 g $NaHCO_3$ 3.0 g $Na_4P_2O_7 \cdot 10H_2O$	Cathodic deposition at -100 mA cm^{-2} for 360 s, 1200 rpm	S5
MoS	0.021g $(NH_4)[MoS_4]$, 0.5616 g $NaClO_4 \cdot H_2O$ Under N_2	Anodic deposition at 0.1 V vs SCE for 288 s, 400 rpm	S6,7
Ni-(a)	12.06 g $NiSO_4 \cdot 6H_2O$, 0.352 g $NiCl_2 \cdot 6H_2O$, 0.113 g H_3BO_3, H_2SO_4 to pH 3.5	Cathodic deposition at -50 mA cm^{-2} for 680 s, 400 rpm	S4
NiCo-(a)	3.2 g $NiSO_4 \cdot 6H_2O$, 0.8 g $CoSO_4 \cdot 7H_2O$, 2 g $K_3C_6H_5O_7 \cdot H_2O$, Na_2CO_3 to pH 10.5	Cathodic deposition at -10 mA cm^{-2} for 5400 s, 400 rpm	S8

NiFe-(a)	4.824 g $NiSO_4 \cdot 6H_2O$, 0.141 g $NiCl_2 \cdot 6H_2O$, 7.206 g $FeSO_4 \cdot 7H_2O$, 0.145 g $FeCl_2 \cdot 4H_2O$, 0.113 g H_3BO_3, H_2SO_4 to pH 3	Cathodic deposition at -50 mA cm^{-2} for 680 s, 400 rpm	S4
NiMo-(a) [a]	3.16 g $NiSO_4 \cdot 6H_2O$, 1.92 g $Na_2MoO_4 \cdot 2H_2O$, 3.52 g $Na_3C_6H_5O_7 \cdot 2H_2O$, excess NH_4OH to pH 10.5[a]	Cathodic deposition at -160 mA cm^{-2} for 1200 s, 800 rpm	S2,9
NiMo-(b)	1.8 g $K_4P_2O_7$, 0.4 g $NiCl_2 \cdot 6H_2O$, 3.0 g $NaHCO_3$ 1.6 g $Na_2MoO_4 \cdot 2H_2O$, NaOH to pH 9	Cathodic deposition at -100 mA cm^{-2} for 900 s, 400 rpm, 60 °C	S10
NiMoCo [a]	2.88 g $NiCl_2 \cdot 6H_2O$, 0.96 g $CoCl_2 \cdot 6H_2O$, 0.96 g $Na_2MoO_4 \cdot 2H_2O$, 4.2 g $Na_3C_6H_5O_7 \cdot 2H_2O$, NH_4OH/NaOH to pH 10.5[a]	Cathodic deposition at -98 mA cm^{-2} for 180 s, 1200 rpm	S11
NiMoFe(a)	3.4 g $NiSO_4 \cdot 6H_2O$, 0.4 g $Na_2MoO_4 \cdot 2H_2O$, 0.4 g $FeSO_4 \cdot 7H_2O$, 2.4 g $K_3C_6H_5O_7 \cdot H_2O$, Na_2CO_3 to pH 10	Cathodic deposition at -10 mA cm^{-2} for 5400 s, 800 rpm,	S12
NiSn(a)	1.12 g $SnCl_2 \cdot 2H_2O$, 1.2 g $NiCl_2 \cdot 6H_2O$, 8 g $K_4P_2O_7$, 0.8 g NH_2CH_2COOH, NH_4OH to pH 8	Cathodic deposition at -100 mA cm^{-2} for 1440 s, 1200 rpm, 55 °C	S13
NiW(a)	3.2 g $NiSO_4 \cdot 6H_2O$, 0.8 g $Na_2WO_4 \cdot 2H_2O$, 2 g $K_3C_6H_5O_7 \cdot H_2O$, Na_2CO_3 to pH 10.5	Cathodic deposition at -10 mA cm^{-2} for 5400 s, 400 rpm,	S8,9

[a]These solutions were made in 40 mL NH_4OH rather than H_2O.

Table S2. Electrodeposited OER Catalysts investigated along with deposition conditions

Catalyst	Deposition Solution (in 40 mL H_2O)	Deposition Conditions	Reference
Co-(b)	0.202 g $CoSO_4 \cdot 7H_2O$ 0.164 g NH_4ClO_4 pH 6.8 w/ NH_4OH	Cathodic deposition at -50 mA cm^{-2} for 30 s,[a] 1200 rpm	S14
Co/B	0.0058 g $Co(NO_3)_2 \cdot 6H_2O$, 0.247 g H_3BO_3, HNO_3 or KOH to pH 9.2	Anodic deposition at 1.049 V vs SCE for 7200 s in quiescent solution	S15
Co/P-(a)	0.0058 g $Co(NO_3)_2 \cdot 6H_2O$, 0.544 g KH_2PO_4, HNO_3 or KOH to pH 7	Anodic deposition at 1.049 V vs SCE for 28800 s in quiescent solution	S16
Co/P-(b)	2.249 g $CoSO_4 \cdot 7H_2O$ 0.428 g NH_4Cl 1.272 g $NaH_2PO_2 \cdot H_2O$ 0.247 g H_3BO_3 0.544 g M $NaOAc \cdot 3H_2O$	Cathodic deposition at -17 mA cm^{-2} for 25560 s, 1200 rpm	S17
CoFe	0.112 g $CoSO_4 \cdot 7H_2O$ 0.100 g $FeSO_4 \cdot 7H_2O$ 0.141 g NH_4ClO_4 NH_4OH to pH 5.4	Cathodic deposition at -250 mA cm^{-2} for 30 s, [a] 1200 rpm	S14
Cu	0.100 g $CuSO_4 \cdot 5H_2O$ 0.141 g NH_4ClO_4 NH_4OH to pH 5.0	Cathodic deposition at -20.5 mA cm^{-2} for 30 s, [a] 1200 rpm	S14
Fe-(b)	0.200 g $FeSO_4 \cdot 7H_2O$ 0.470 g NH_4ClO_4 H_2SO_4 to pH 1.5	Cathodic deposition at -92.3 mA cm^{-2} for 30 s, [a] 1200 rpm	S14
FeMn	0.100 g $FeSO_4 \cdot 7H_2O$ 0.061 g $MnSO_4 \cdot H_2O$ 0.411 g NH_4ClO_4 H_2SO_4 to pH 2.5	Cathodic deposition at -61.53 mA cm^{-2} for 30 s, [a] 1200 rpm	S14
Ni-(b)	1.047 g $Ni(NO_3)_2 \cdot 6\ H_2O$	Cathodic deposition at -16 mA cm^{-2} for 10 s, 800 rpm	S18
Ni/B	0.0116 g $Ni(NO_3)_2 \cdot 6H_2O$, 0.247 g H_3BO_3, HNO_3 or KOH to pH 9.2 Filtered through 0.4um filterdisc before use	Anodic deposition at 1.049 V vs SCE for 8400 s in quiescent solution	S19
NiCe	1.047 g $Ni(NO_3)_2 \cdot 6H_2O$ 0.174 g $Ce(NO_3)_3 \cdot 6H_2O$	Cathodic deposition at -16 mA cm^{-2} for 10 s, 1200 rpm	S18
NiCo-(b)	1.047 g $Ni(NO_3)_2 \cdot 6H_2O$ 0.116 g $Co(NO_3)_2 \cdot 6H_2O$	Cathodic deposition at -16 mA cm^{-2} for 10 s, 1200 rpm	S18
NiCo-(c)	2.63 g $NiSO_4 \cdot 6H_2O$ 2.81 g $CoSO_4 \cdot 7H_2O$ 6.44g $Na_2SO_4 \cdot 10H_2O$ 1.24 g H_3BO_3	Cathodic deposition at -50 mA cm^{-2} for 50 s, 400 rpm	S20
NiCr	0.095 g $NiSO_4 \cdot 6H_2O$ 0.141 g $Cr_2(SO_4)_3 \cdot H_2O$ 0.132 g NH_4SO_4	Cathodic deposition at -51.28 mA cm^{-2} for 50 s, [b] 1200 rpm	S21

NiCu	1.047 g $Ni(NO_3)_2 \cdot 6H_2O$ 0.118 g $Cu(NO_3)_2 \cdot 6H_2O$	Cathodic deposition at -16 mA cm^{-2} for 10 s, 400 rpm	S14
NiFe-(b)	0.095 g $NiSO_4 \cdot 6H_2O$ 0.100 g $FeSO_4 \cdot 7H_2O$ 0.117 g NH_4ClO_4 NH_4OH/H_2SO_4 to pH 2.5	Cathodic deposition at -50 mA cm^{-2} for 50 s,[a] 1200 rpm	S14
NiFe-(c)	1.047 g $Ni(NO_3)_2 \cdot 6H_2O$ 0.162 g $Fe(NO_3)_2 \cdot 9H_2O$ HNO_3 to pH 2	Cathodic deposition at -8 mA cm^{-2} for 100 s, 400 rpm	S22
NiLa	1.047 g $Ni(NO_3)_2 \cdot 6H_2O$ 0.173 g $La(NO_3)_3 \cdot 6H_2O$	Cathodic deposition at -16 mA cm^{-2} for 10 s, 1200 rpm	S18
NiMoFe(b)	0.243 g $NiSO_4 \cdot 6H_2O$ 0.257 g $NiCl_2 \cdot 6H_2O$ 0.040 g $Na_2MoO_4 \cdot 2H_2O$ 0.040 g $FeSO_4 \cdot 7H_2O$ 0.240 g $K_3C_6H_5O_7 \cdot H_2O$ 0.32 g $(NH_4)_2CO_3$ pH 7	Cathodic deposition at -61.5 mA cm^{-2} for 600 s, 1200 rpm	S23
NiSn(b)	2.377 g $NiCl_2 \cdot 6H_2O$ 0.072 g $SnCl_2 \cdot 2H_2O$ 3.003 g NH_2CH_2COOH 6.607 g $K_4P_2O_7$ pH 8	Cathodic deposition at -10 mA cm^{-2} for 900 s, 1200 rpm	S24
NiZn(b)	15.830 g $NiSO_4 \cdot 6H_2O$ 0.499 g $ZnSO_4 \cdot 7H_2O$ 3.301 g $NiCl_2 \cdot 6H_2O$ 1.2 g H_3BO_3 pH 4.7	Cathodic deposition at -20 mA cm^{-2} for 2700 s, 1200 rpm Then immerse in 28% KOH for 24 h	S24
Ru-(a)	0.450 g $RuCl_3 \cdot H_2O$ 2.98 g KCl 0.01 M HCl	100 CVs from 0.06 to 0.96 V vs SCE at 0.05 V/s scan rate Then anneal in air at 200 °C for 3 h	S25

[a]The reported cathodic deposition current density of these materials on Pt discs was -250 mA cm^{-2}. The large reported deposition current density may be due to background H_2-evolution by the Pt substrate. We were unable to attain this current density when depositing onto GC disks, and instead deposited at the current densities listed.

Section 3: Summary of HER/OER Activity, Stability, and ECSA data

Table S3 HER Activity – 1 M H_2SO_4

Catalyst	RF	$\eta_{t=0}$ / V	$\eta_{t=2h}$ / V	$\lvert j_{g,\ \eta=0.1\ V}\rvert$ / mA cm^{-2}	$\lvert j_{s,\ \eta=0.1\ V}\rvert$ / mA cm^{-2}
Co-(a)	600 ± 300	-0.23 ± 0.03	-0.26 ± 0.04	-[a]	-[a]
CoMo	1100 ± 600	-0.10 ± 0.02	-0.10 ± 0.01	4.6 ± 2.6	0.004 ± 0.003
CoNiFe	90 ± 50	-0.37 ± 0.03	-0.40 ± 0.03	< 0.1	< 0.001
CoW	300 ± 200	-0.18 ± 0.02	-0.18 ± 0.02	1.2 ± 0.6	0.004 ± 0.003
Fe-(a)	0.9 ± 0.2	-0.74 ± 0.11	-0.85 ± 0.06	< 0.1	< 0.001
FeMo	300 ± 200	-0.23 ± 0.04	-0.23 ± 0.02	< 0.1	< 0.001
Mo/S	26 ± 3	-0.22 ± 0.01	-0.25 ± 0.03	0.32 ± 0.17	0.013 ± 0.007
Ni-(a)	20 ± 10	-0.37 ± 0.04	-0.47 ± 0.09	< 0.1	< 0.001
NiCo-(a)	600 ± 300	-0.16 ± 0.03	-0.18 ± 0.01	-[b]	-[b]
NiFe-(a)	1400 ± 300	-0.22 ± 0.06	-0.26 ± 0.03	-[a]	-[a]
NiMo-(a)	1200 ± 500	-0.045 ± 0.004	-0.039 ± 0.003	91 ± 46	0.074 ± 0.048
NiMo-(b)	1000 ± 500	-0.11 ± 0.02	-0.12 ± 0.02	7.2 ± 3.9	0.007 ± 0.005
NiMoCo	1200 ± 500	-0.05 ± 0.01	-0.05 ± 0.01	53 ± 25	0.043 ± 0.028
NiMoFe-(a)	700 ± 200	-0.09 ± 0.01	-0.10 ± 0.01	10 ± 3	0.014 ± 0.006
NiSn-(a)	500 ± 100	-0.39 ± 0.09	-0.48 ± 0.07	< 0.1	< 0.001
NiW	1200 ± 600	-0.06 ± 0.02	-0.11 ± 0.05	17 ± 11	0.014 ± 0.011
Pt-(a)	6 ± 2	-0.05 ± 0.01	-0.08 ± 0.01	110 ± 70	19 ± 14
Pt-(b)	90 ± 20	-0.05 ± 0.01	-0.06 ± 0.01	220 ± 80	2.5 ± 1.1
GC Background	7 ± 4	-1.10 ± 0.14	-0.90 ± 0.02	< 0.1	< 0.002

[a]This material was investigated at potentials negative of -0.44 V vs SCE due to anodic dissolution occurring at more positive potentials. [b]This material was investigated at potentials negative of -0.40 V vs SCE due to anodic dissolution occurring at more positive potentials.

Table S4 HER Activity – 1 M NaOH

Catalyst	RF	$\eta_{t=0}$ / V	$\eta_{t=2h}$ / V	$\lvert j_{g,\ \eta=0.35\ V}\rvert$ / mA cm^{-2}	$\lvert j_{s,\ \eta=0.35\ V}\rvert$ / mA cm^{-2}
Co-(a)	1100 ± 400	-0.22 ± 0.02	-0.22 ± 0.02	2.3 ± 1.2	0.002 ± 0.001
CoMo	700 ± 400	-0.10 ± 0.02	-0.10 ± 0.02	10.4 ± 3.7	0.014 ± 0.008
CoNiFe	110 ± 30	-0.25 ± 0.02	-0.22 ± 0.02	0.3 ± 0.1	0.003 ± 0.002
CoW	700 ± 200	-0.22 ± 0.01	-0.20 ± 0.03	0.8 ± 0.3	0.001 ± 0.0005
Fe-(a)	670 ± 50	-0.13 ± 0.01	-0.27 ± 0.06	2.8 ± 1.4	0.004 ± 0.002
FeMo	400 ± 200	-0.22 ± 0.03	-0.23 ± 0.04	0.4 ± 0.3	< 0.001
Mo/S	10 ± 5	-0.57 ± 0.09	-0.48 ± 0.01	0.2 ± 0.1	0.017 ± 0.013
Ni-(a)	16 ± 2	-0.26 ± 0.04	-0.29 ± 0.03	0.3 ± 0.1	0.021 ± 0.010
NiCo-(a)	17 ± 5	-0.21 ± 0.02	-0.24 ± 0.04	1.0 ± 0.2	0.062 ± 0.023
NiFe-(a)	4000 ± 1000	-0.09 ± 0.04	-0.12 ± 0.02	6.5 ± 2.3	0.002 ± 0.001
NiMo(a)	800 ± 400	-0.04 ± 0.02	-0.03 ± 0.01	35 ± 20	0.047 ± 0.038
NiMo(b)	1000 ± 700	-0.07 ± 0.02	-0.10 ± 0.03	20 ± 5	0.020 ± 0.014
NiMoCo	900 ± 400	-0.07 ± 0.03	-0.09 ± 0.04	19 ± 11	0.020 ± 0.015
NiMoFe-(a)	900 ± 400	-0.13 ± 0.02	-0.13 ± 0.03	3.2 ± 0.9	0.003 ± 0.002
NiSn-(a)	17 ± 6	-0.41 ± 0.03	-0.36 ± 0.02	< 0.1	< 0.001
NiW	900 ± 500	-0.20 ± 0.03	-0.20 ± 0.05	1.6 ± 0.7	0.002 ± 0.001
Pt-(a)	10 ± 4	-0.10 ± 0.02	-0.19 ± 0.06	12 ± 4	1.2 ± 0.7
Pt-(b)	130 ± 50	-0.03 ± 0.01	-0.06 ± 0.02	70 ± 20	0.54 ± 0.28
GC Background	4 ± 3	-0.70 ± 0.02	-0.47 ± 0.02	< 0.1	< 0.001

Table S5 OER Activity – 1 M H_2SO4

Catalyst	RF	$\eta_{t=0}$ / V	$\eta_{t=2h}$ / V	$j_{g,\ \eta=0.35\ V}$ / mA cm^{-2}	$j_{s,\ \eta=0.35\ V}$ / mA cm^{-2}
Co-(b)	11 ± 5	1.07 ± 0.01	1.12 ± 0.01	< 0.1	< 0.01
Co/B	9 ± 1	1.08 ± 0.02	1.13 ± 0.01	< 0.1	< 0.01
Co/P-(a)	13 ± 4	1.06 ± 0.02	1.12 ± 0.02	< 0.1	< 0.01
Co/P-(b)	13 ± 3	1.08 ± 0.01	1.13 ± 0.01	< 0.1	< 0.01
CoFe	11 ± 4	1.06 ± 0.01	1.11 ± 0.01	< 0.1	< 0.01
Cu	9 ± 1	1.09 ± 0.01	1.12 ± 0.02	< 0.1	< 0.01
Fe(b)	9 ± 4	1.11 ± 0.02	1.14 ± 0.01	< 0.1	< 0.01
FeMn	8 ± 2	1.09 ± 0.02	1.14 ± 0.01	< 0.1	< 0.01
Ir	160 ± 20	0.34 ± 0.01	0.36 ± 0.02	13.7 ± 5.0	0.09 ± 0.03
Ni(b)	13 ± 4	1.04 ± 0.07	1.10 ± 0.04	< 0.1	< 0.01
Ni/B	6 ± 2	1.09 ± 0.03	1.15 ± 0.04	< 0.1	< 0.01
NiCe	7 ± 1	1.10 ± 0.02	1.12 ± 0.01	< 0.1	< 0.01
NiCo-(b)	5 ± 1	1.08 ± 0.03	1.13 ± 0.01	< 0.1	< 0.01
NiCo-(c)	5 ± 2	1.10 ± 0.01	1.12 ± 0.01	< 0.1	< 0.01
NiCr	10 ± 3	1.07 ± 0.01	1.12 ± 0.01	< 0.1	< 0.01
NiCu	7 ± 2	1.07 ± 0.02	1.12 ± 0.02	< 0.1	< 0.01
NiFe-(b)	10 ± 5	1.08 ± 0.03	1.12 ± 0.01	< 0.1	< 0.01
NiFe-(c)	9 ± 1	1.06 ± 0.01	1.12 ± 0.01	< 0.1	< 0.01
NiLa	7 ± 2	1.08 ± 0.03	1.12 ± 0.01	< 0.1	< 0.01
NiMoFe-(b)	25 ± 6	1.05 ± 0.02	1.12 ± 0.04	< 0.1	< 0.01
NiSn-(b)	2300 ± 500	0.14 ± 0.10	1.17 ± 0.07	< 0.1	< 0.01
NiZn	15 ± 4	1.05 ± 0.02	1.13 ± 0.01	< 0.1	< 0.01
Ru-(a)	71 ± 8	0.28 ± 0.03	0.34 ± 0.05	29.8 ± 8.8	0.42 ± 0.13
Ru-(b)	110 ± 30	0.29 ± 0.01	0.36 ± 0.05	53.3 ± 14.0	0.47 ± 0.19
GC Background	7 ± 4	1.11 ± 0.01	1.14 ± 0.04	< 0.1	< 0.01

Note that all materials except for Ir, NiSn-(b), Ru-(a), and Ru-(b) showed approximately equivalent activity, stability, and roughness factor to that measured for the bare glassy carbon background.

Table S6 OER Activity – 1 M NaOH

Catalyst	RF	$\eta_{t=0}$ / V	$\eta_{t=2h}$ / V	$j_{g,\,\eta=0.35\,V}$ / mA cm^{-2}	$j_{s,\,\eta=0.35\,V}$ / mA cm^{-2}
Co-(b)	11 ± 5	0.41 ± 0.03	0.40 ± 0.04	0.6 ± 0.3	0.05 ± 0.04
Co/B	22 ± 2	0.42 ± 0.03	0.43 ± 0.05	0.5 ± 0.3	0.02 ± 0.01
Co/P-(a)	17 ± 9	0.39 ± 0.02	0.38 ± 0.02	0.6 ± 0.4	0.04 ± 0.03
Co/P-(b)	80 ± 50	0.38 ± 0.02	0.36 ± 0.02	3.5 ± 1.4	0.04 ± 0.03
CoFe	10 ± 3	0.35 ± 0.01	0.36 ± 0.01	5.2 ± 1.8	0.53 ± 0.24
Cu	6 ± 2	0.97 ± 0.25	1.27 ± 0.02	< 0.1	< 0.01
Fe(b)	6 ± 3	0.50 ± 0.01	1.27 ± 0.01	< 0.1	< 0.01
FeMn	6 ± 2	0.63 ± 0.03	1.24 ± 0.06	< 0.1	< 0.01
Ir	130 ± 10	0.39 ± 0.01	0.43 ± 0.02	2.9 ± 0.7	0.02 ± 0.01
Ni-(b)	2 ± 1	0.47 ± 0.04	0.47 ± 0.03	0.7 ± 0.4	0.34 ± 0.23
Ni/B	4 ± 1	0.46 ± 0.02	0.47 ± 0.03	0.5 ± 0.2	0.12 ± 0.07
NiCe	4 ± 1	0.45 ± 0.03	0.51 ± 0.05	1.9 ± 0.7	0.42 ± 0.17
NiCo-(b)	3 ± 2	0.42 ± 0.02	0.42 ± 0.03	1.0 ± 0.3	0.31 ± 0.21
NiCo-(c)	9 ± 4	0.38 ± 0.01	0.35 ± 0.01	2.0 ± 0.8	0.24 ± 0.14
NiCr	9 ± 3	0.39 ± 0.02	0.39 ± 0.02	1.8 ± 1.0	0.20 ± 0.12
NiCu	7 ± 3	0.49 ± 0.05	0.50 ± 0.05	0.6 ± 0.3	0.08 ± 0.06
NiFe-(b)	4 ± 1	0.34 ± 0.02	0.37 ± 0.02	10.9 ± 6.0	2.78 ± 1.65
NiFe-(c)	4 ± 1	0.38 ± 0.01	0.40 ± 0.01	3.9 ± 0.6	1.05 ± 0.30
NiFeCoCe-(a)	13 ± 7	0.35 ± 0.01	0.35 ± 0.02	4.7 ± 1.0	0.36 ± 0.22
NiFeCoCe-(b)	21 ± 2	0.36 ± 0.01	0.36 ± 0.01	4.3 ± 0.7	0.20 ± 0.04
NiLa	4 ± 1	0.47 ± 0.04	0.47 ± 0.03	1.2 ± 0.5	0.29 ± 0.14
NiMoFe-(b)	9 ± 3	0.34 ± 0.02	0.33 ± 0.02	18.6 ± 10.4	2.1 ± 1.4
NiSn(b)	14 ± 3	0.39 ± 0.01	0.36 ± 0.03	2.1 ± 1.1	0.15 ± 0.09
NiZn	200 ± 100	0.36 ± 0.02	0.35 ± 0.03	6.3 ± 3.1	0.03 ± 0.02
Ru-(a)	70 ± 20	0.29 ± 0.03	0.32 ± 0.02	32.4 ± 14.3	0.49 ± 0.24
Ru-(b)	200 ± 20	0.34 ± 0.03	0.40 ± 0.04	17.5 ± 7.5	0.09 ± 0.04
GC Background	4 ± 3	1.21 ± 0.04	1.25 ± 0.01	< 0.1	< 0.01

Section S4: Representative ECSA measurements for NiMo-(a) and Ni-(a)

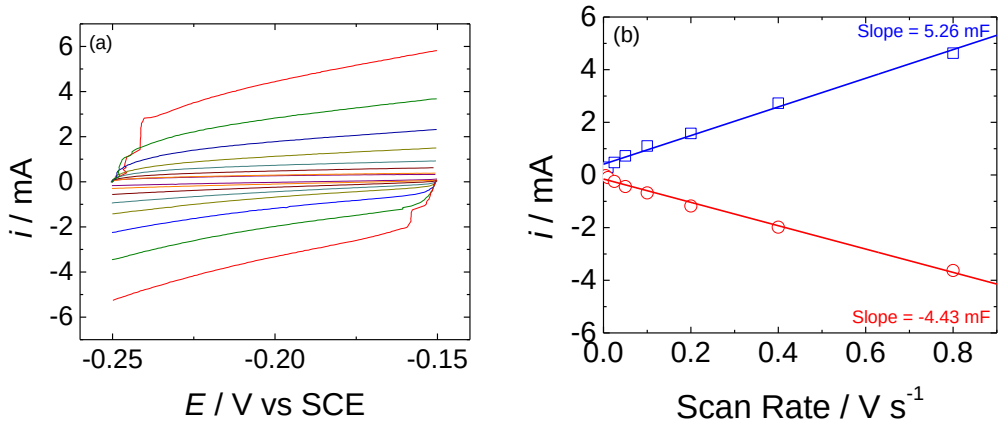

Figure S2. Double-layer capacitance measurements for determining electrochemically-active surface area of NiMo-(a) in 1 M H_2SO_4. (a) Cyclic voltammograms were measured in a non-Faradaic region of the voltammogram at the following scan rate: (—) 0.005 (—) 0.01, (—) 0.025, (—) 0.05, (—) 0.1, (—) 0.2, (—) 0.4, and (—) 0.8 V/s. The working electrode was held at each potential vertex for 10 s before the beginning the next sweep. All current is assumed to be due to capacitive charging. (b) The cathodic (○) and anodic (□) charging currents measured at -0.20 V vs. SCE plotted as a function of scan rate. The double-layer capacitance of the system is taken as the average of the absolute value of the slope of the linear fits to the data. A roughness factor of RF = 710 is estimated from the above measurements.

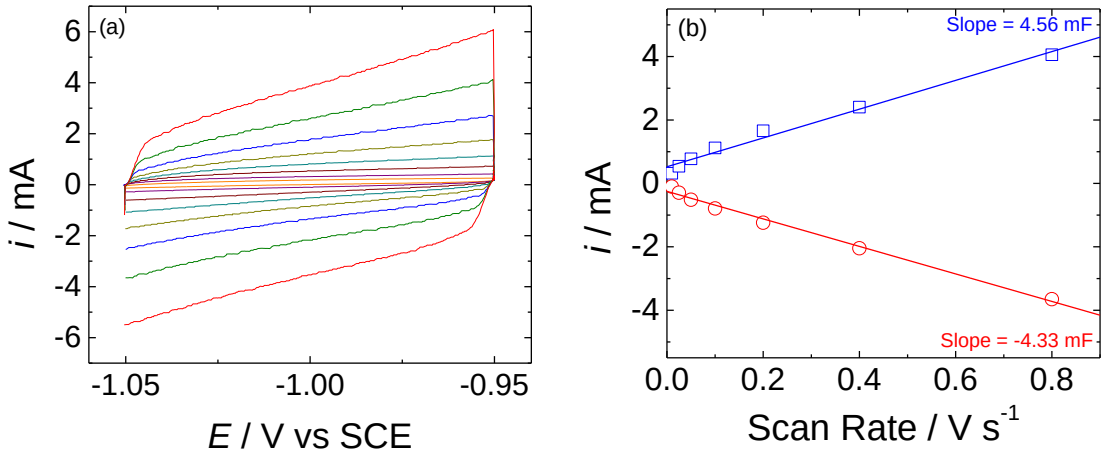

Figure S3. Double-layer capacitance measurements for determining electrochemically-active surface area of NiMo-(a) in 1 M NaOH. (a) Cyclic voltammograms were measured in a non-Faradaic region of the voltammogram at the following scan rate: (—) 0.005 (—) 0.01, (—) 0.025, (—) 0.05, (—) 0.1, (—) 0.2, (—) 0.4, and (—) 0.8 V/s. The working electrode was held at each potential vertex for 10 s before the beginning the next sweep. All current is assumed to be due to capacitive charging. (b) The cathodic (○) and anodic (□) charging currents measured at -1.0 V vs. SCE plotted as a function of scan rate. The double-layer capacitance of the system is taken as the average of the absolute value of the slope of the linear fits to the data. A roughness factor of RF = 570 is estimated from the above measurements.

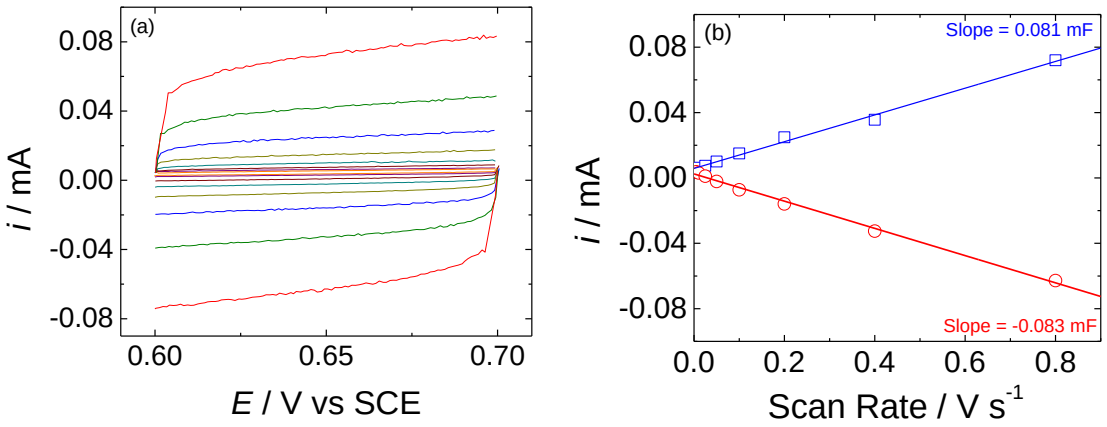

Figure S4. Double-layer capacitance measurements for determining electrochemically-active surface area of Co-(b) in 1 M H_2SO_4. (a) Cyclic voltammograms were measured in a non-Faradaic region of the voltammogram at the following scan rate: (—) 0.005 (—) 0.01, (—) 0.025, (—) 0.05, (—) 0.1, (—) 0.2, (—) 0.4, and (—) 0.8 V/s. The working electrode was held at each potential vertex for 10 s before the beginning the next sweep. All current is assumed to be due to capacitive charging. (b) The cathodic (○) and anodic (□) charging currents measured at -0.65 V vs. SCE plotted as a function of scan rate. The double-layer capacitance of the system is taken as the average of the absolute value of the slope of the linear fits to the data. A roughness factor of RF = 12 is estimated from the above measurements.

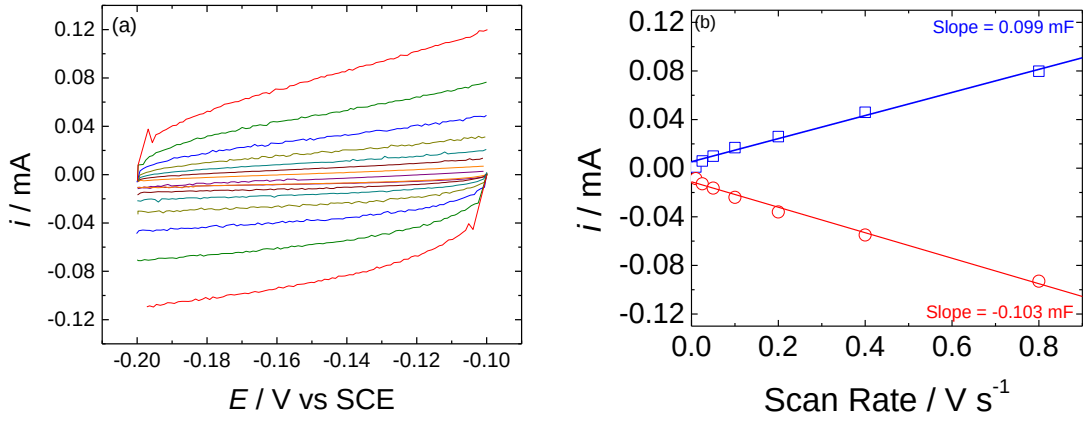

Figure S5. Double-layer capacitance measurements for determining electrochemically-active surface area of Co-(b) in 1 M NaOH. (a) Cyclic voltammograms were measured in a non-Faradaic region of the voltammogram at the following scan rate: (—) 0.005 (—) 0.01, (—) 0.025, (—) 0.05, (—) 0.1, (—) 0.2, (—) 0.4, and (—) 0.8 V/s. The working electrode was held at each potential vertex for 10 s before the beginning the next sweep. All current is assumed to be due to capacitive charging. (b) The cathodic (○) and anodic (□) charging currents measured at -0.15 V vs. SCE plotted as a function of scan rate. The double-layer capacitance of the system is taken as the average of the absolute value of the slope of the linear fits to the data. A roughness factor of RF = 13 is estimated from the above measurements.

Section S5: Representative HER/OER activity, stability and Faradaic efficiency measurements for NiMo-(a) and Co-(b)

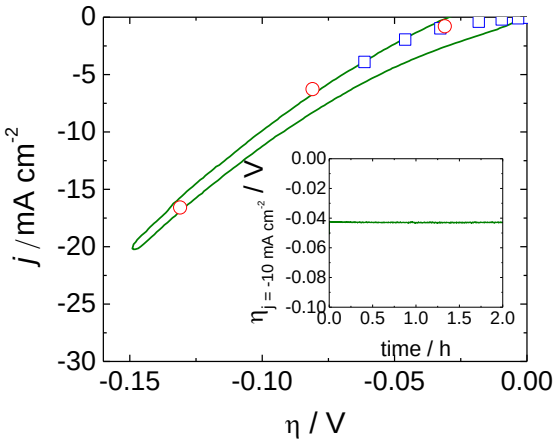

Figure S6. Representative rotating disk voltammogram of HER at NiMo-(a) in H_2-saturated 1 M H_2SO_4 at 0.01 V scan rate and 1600 rpm. The results of 30 s chronopotentiometric steps (blue squares) and chronoamperometric steps (red circles) are shown for comparison, and the close overlay of the data suggests good approximation of steady-state conditions. The inset is a representative 2-h controlled-current electrolysis at 10 mA cm^{-2} per geometric area for the same material under identical conditions.

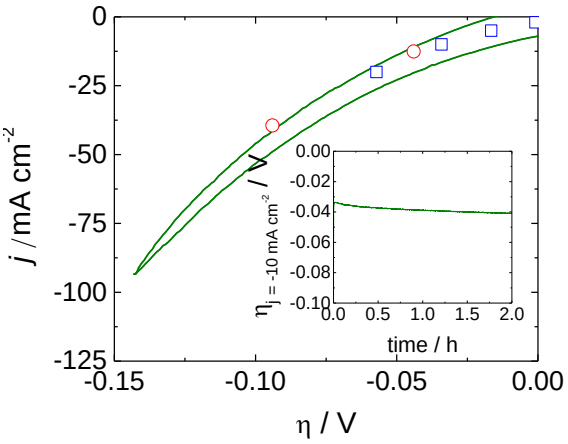

Figure S7. Representative rotating disk voltammogram of HER at NiMo-(a) in H_2-saturated 1 M NaOH at 0.01 V scan rate and 1600 rpm. The results of 30 s chronopotentiometric steps (blue squares) and chronoamperometric steps (red circles) are shown for comparison, and the close overlay of the data suggests good approximation of steady-state conditions. The inset is a representative 2-h controlled-current electrolysis at 10 mA cm^{-2} per geometric area for the same material under identical conditions.

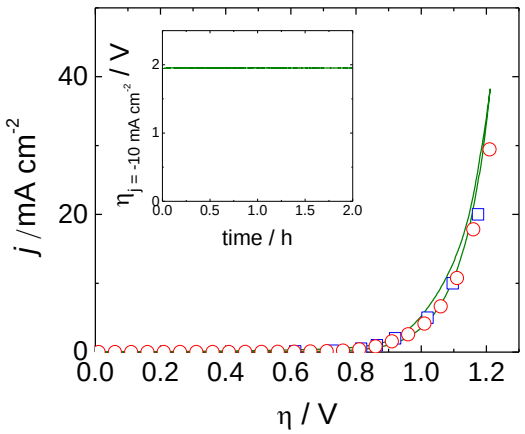

Figure S8. Representative rotating disk voltammogram of OER at Co-(b) in O_2-saturated 1 M H_2SO_4 at 0.01 V scan rate and 1600 rpm. The results of 30 s chronopotentiometric steps (blue squares) and chronoamperometric steps (red circles) are shown for comparison, and the close overlay of the data suggests good approximation of steady-state conditions. The inset is a representative 2-h controlled-current electrolysis at 10 mA cm^{-2} per geometric area for the same material under identical conditions. Note that the activity and stability data here is equivalent to that for a bare glassy carbon electrode in 1 M H_2SO_4.

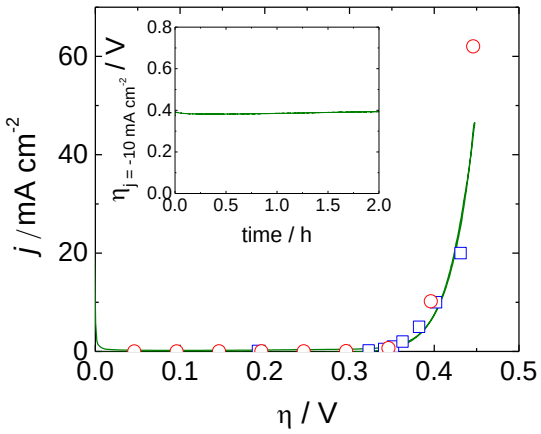

Figure S9. Representative rotating disk voltammogram of OER at Co-(b) in O_2-saturated 1 M NaOH at 0.01 V scan rate and 1600 rpm. The results of 30 s chronopotentiometric steps (blue squares) and chronoamperometric steps (red circles) are shown for comparison, and the close overlay of the data suggests good approximation of steady-state conditions. The inset is a representative 2-h controlled-current electrolysis at 10 mA cm^{-2} per geometric area for the same material under identical conditions.

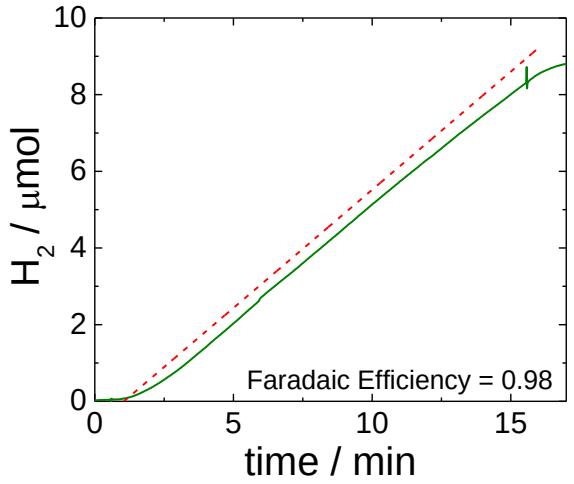

Figure S10. Representative Faradaic efficiency measurement for HER by NiMo-(a) in 1 M H_2SO_4. Measurements were conducted in the two-compartment bulk electrolysis cell shown in Figure S1 with no headspace—all gaseous products were dissolved in solution. The electrode was held at -10 mA cm^{-2} current density for 15 minutes at a 0.195 cm^2 disk electrode. The amount of H_2 expected from the amount of charge passed (1.755 C) assuming 100% Faradaic efficiency is shown as a dashed red line. The amount of H_2 detected by the Unisense H_2-500 probe is shown as a solid green line. The determined Faradaic efficiency for this experiment was $\varepsilon = 0.98$.

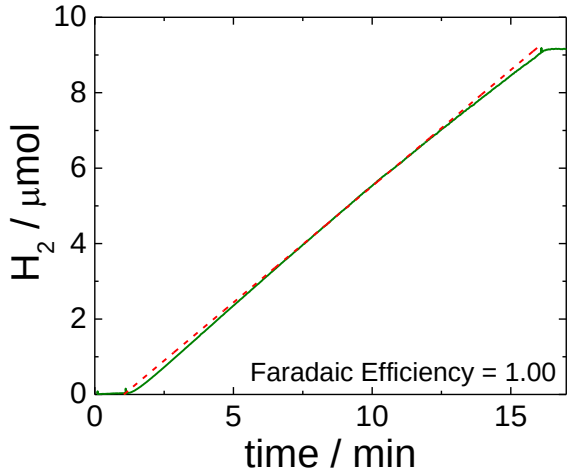

Figure S11. Representative Faradaic efficiency measurement for HER by NiMo-(a) in 1 M NaOH. Measurements were conducted in the two-compartment bulk electrolysis cell shown in Figure S1 with no headspace—all gaseous products were dissolved in solution. The electrode was held at -10 mA cm^{-2} current density for 15 minutes at a 0.195 cm^2 disk electrode. The amount of H_2 expected from the amount of charge passed (1.755C) assuming 100% Faradaic efficiency is shown as a dashed red line. The amount of H_2 detected by the Unisense H_2-500 probe is shown as a solid green line. The determined Faradaic efficiency for this experiment was $\varepsilon = 1.00$.

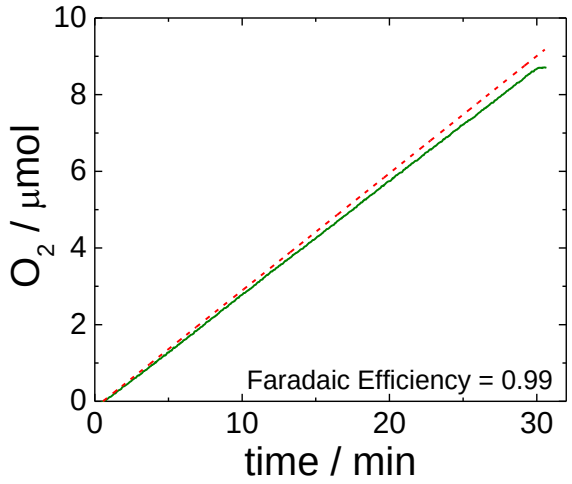

Figure S12. Representative Faradaic efficiency measurement for HER by Co-(b) in 1 M NaOH. Measurements were conducted in the two-compartment bulk electrolysis cell shown in Figure S1 with no headspace—all gaseous products were dissolved in solution. The electrode was held at 10 mA cm^{-2} current density for 30 minutes at a 0.195 cm^2 disk electrode. The amount of O_2 expected from the amount of charge passed (3.510 C) assuming 100% Faradaic efficiency is shown as a dashed red line. The amount of O_2 detected by the Unisense Ox-500 probe is shown as a solid green line. The determined Faradaic efficiency for this experiment was $\varepsilon = 0.99$.

Section S6: Representative 24-h OER stability and Faradaic Efficiency measurements for Co/P-(b)

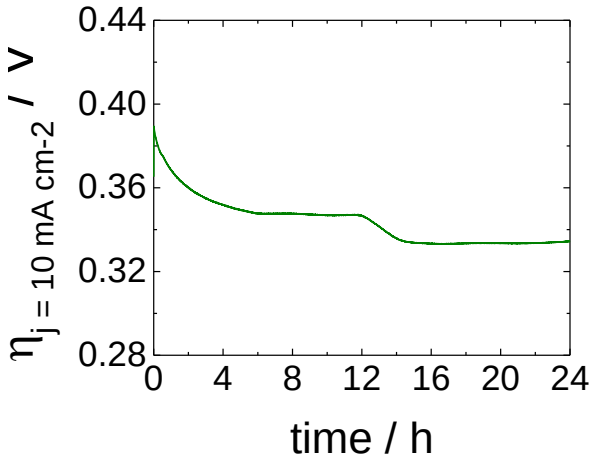

Figure S13. Representative 24-h chronopotentiometric steps of Co/P-(b) held at 10 mA cm^{-2} in 1 M NaOH. In general, each 24-h measurements showed a decrease in operating overpotential at 10 mA cm^{-2} in the first 16-h of the experiment, consistent with a catalyst activation step. This suggests that some portion of the current is going towards catalysts activation, and may explain the low Faradaic efficiency for OER of the as-deposited film.

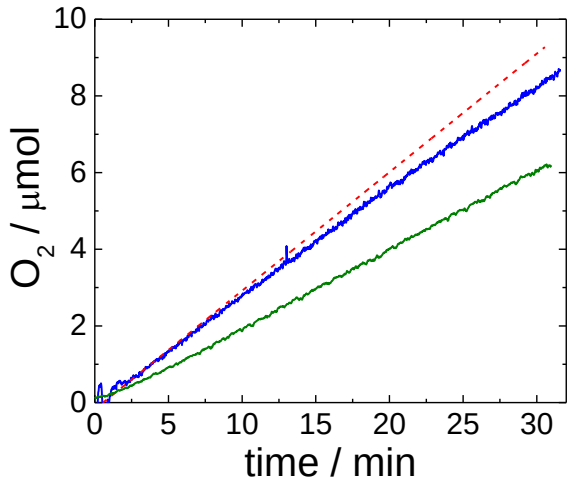

Figure S14. Representative Faradaic efficiency measurements for OER by Co/P-(b) in 1 M NaOH. Measurements were conducted in the two-compartment bulk electrolysis cell shown in Figure S1 with no headspace—all gaseous products were dissolved in solution. The electrode was held at 10 mA cm^{-2} current density for 30 minutes at a 0.195 cm^2 disk electrode. The amount of O_2 expected from the amount of charge passed (3.510 C) assuming 100% Faradaic efficiency is shown as a dashed red line. The amount of O_2 detected by the Unisense Ox-500 probe for an as-deposited Co/P-(b) catalyst is shown in the solid green line, and for a Co/P-(b) after 24-h of constant polarization at 10 mA cm^{-2} is shown in the solid blue line. The determined Faradaic efficiencies an as-deposited catalyst and a catalyst after 24-h constant polarization are $\varepsilon = 0.69$ and $\varepsilon = 0.94$, respectively.

Section S7: Representative 24-h Stability measurements for Co-(b), and NiCr

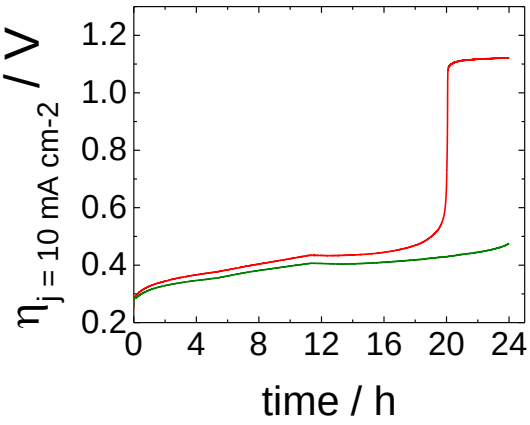

Figure S15. Representative 24-h chronopotentiometric steps of Ru-(a) held at 10 mA cm^{-2} in 1 M H_2SO_4. Of the 7 experiments conducted, 4 showed the same rapid loss of activity as that shown in the red trace. The other 3 showed good stability over the course of 24-h a shown in the green trace. These results suggest that the film would be unstable to longer (>24 h) constant polarization measurements.

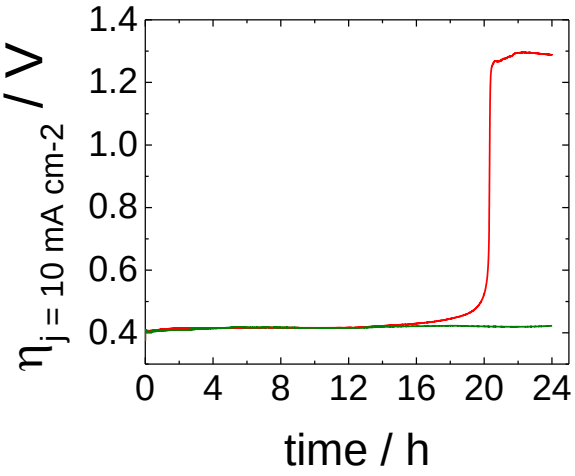

Figure S16. Representative 24-h chronopotentiometric steps of Co-(b) held at 10 mA cm^{-2} in 1 M NaOH. Of the 7 experiments conducted, 3 showed the same rapid loss of activity as that shown in the red trace. The other 4 showed good stability over the course of 24-h similar to that shown in the green trace. . These results suggest that the film would be unstable to longer (>24 h) constant polarization measurements.

.

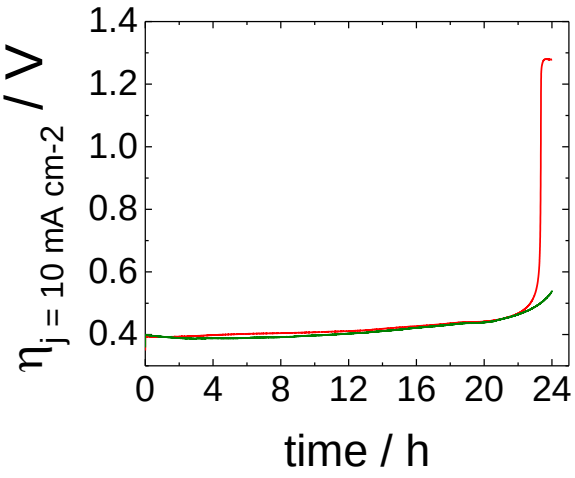

Figure S17. Representative 24-h chronopotentiometric steps of NiCr held at 10 mA cm^{-2} in 1 M NaOH. Of the 7 experiments conducted, 4 showed the same rapid loss of activity as that shown in the red trace. The other 3 showed good stability over the course of 24-h similar to that shown in the green trace. Note that green trace also shows the onset of loss of catalytic activity at ~ 22 h. These results suggest that the film would be unstable to longer (>24 h) constant polarization measurements.

Section S8: Potential Cycling Experiments for Accelerated Durability Testing of NiMo-(a)

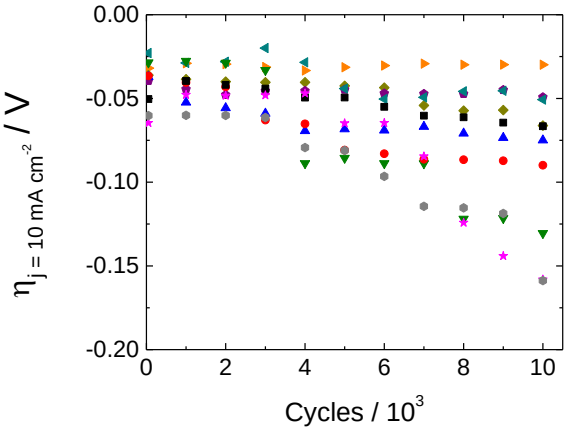

Figure S18. Potential cycling stability study for NiMo-(a) in 1 M H_2SO_4. Each symbol represents the measured overpotential at 10 mA cm^{-2} current density from intermittent 30s chronopotentiometric steps during an independent 10,000 cycle experiment plotted vs the number of cycles on the bottom x-axis. The average initial operating overpotential is $\eta_{t=0}$ = -0.042 ± 0.013, and it changes after 10,000 cycles to $\eta_{10,000\ cycles}$ = -0.087 ± 0.046.

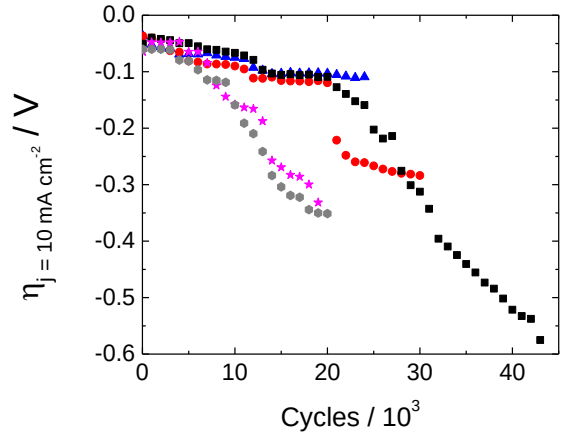

Figure S19. Extended potential cycling stability study for NiMo-(a). Each symbol represents the measured overpotential at 10 mA cm^{-2} current density from intermittent 30s chronopotentiometric steps during an independent > 20,000 cycle experiment plotted vs the number of cycles on the bottom x-axis.

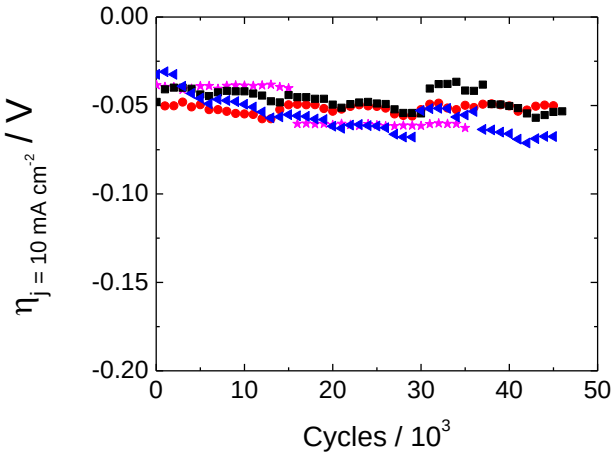

Figure S20. Extended potential cycling stability study for NiMo-(a) in 1 M NaOH. Each symbol represents the measured overpotential at 10 mA cm^{-2} current density from intermittent 30s chronopotentiometric steps during an independent > 20,000 cycle experiment plotted vs the number of cycles on the bottom x-axis. The average initial operating overpotential is $\eta_{t=0}$ = -0.039 ± 0.08, and it changes after 10,000 cycles to $\eta_{10,000\ cycles}$ = -0.046 ± 0.007 and after 40,000 cycles to $\eta_{40,000\ cycles}$ = -0.055 ± 0.009.

Section S9: XPS Spectra of HER Materials

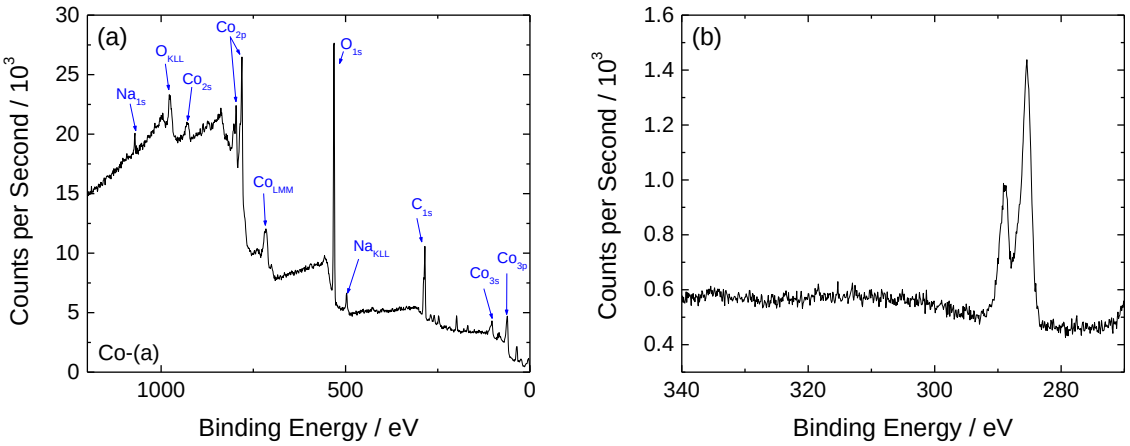

Figure S21. XPS of electrodeposited Co-(a) on glassy carbon. (a) XPS survey scans with XPS and Auger peaks assigned as labeled. Small peaks at 35 eV and 197 eV are not labeled, but are assigned as Na 2p and Cl 2p peaks, respectively. Note that the presence of Na and Cl is likely due to adsorbed ions from the deposition bath. (b) High resolution scans of the Ir4d/Pt4d/Ru3d region. The peak at 284.3 eV is the expected C1s peak for graphitic carbon in glassy carbon,[S26,27] and the small peak at 287.7 eV is typical for more oxidized carbon groups on an anodized carbon surface.[S26,28] No other peaks are evident in this region.

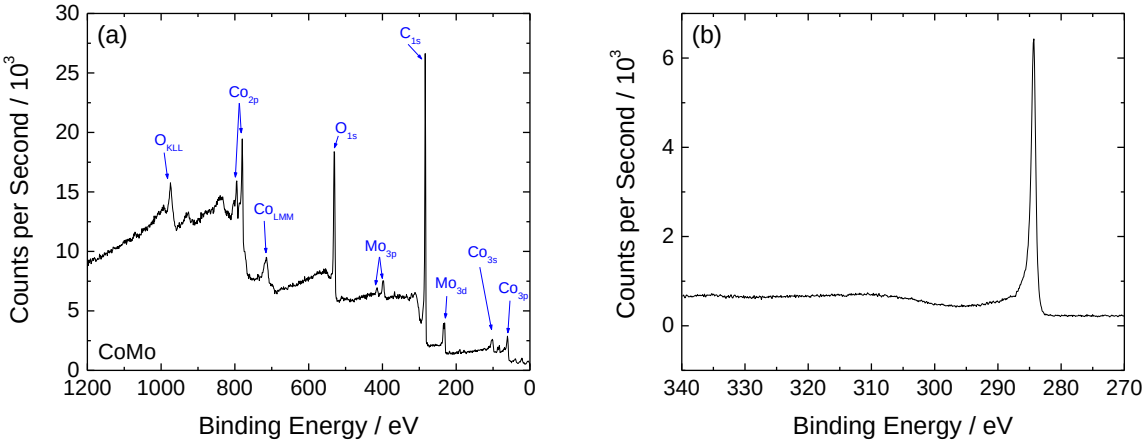

Figure S22. XPS of electrodeposited CoMo on glassy carbon. (a) XPS survey scans with XPS and Auger peaks assigned as labeled. (b) High resolution scans of the Ir4d/Pt4d/Ru3d region. The peak at 284.3 eV is the expected C1s peak for graphitic carbon in glassy carbon.[S26,27] No other peaks are evident in this region.

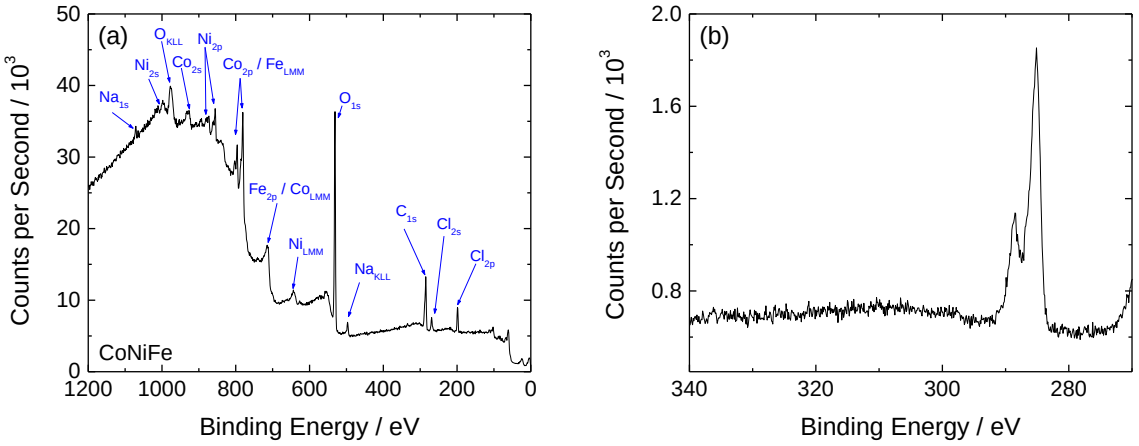

Figure S23. XPS of electrodeposited CoNiFe on glassy carbon. (a) XPS survey scans with XPS and Auger peaks assigned as labeled. Note that the presence of Na and Cl is likely due to adsorbed ions from the deposition bath. (b) High resolution scans of the Ir4d/Pt4d/Ru3d region. The peak at 284.3 eV is the expected C1s peak for graphitic carbon in glassy carbon,[S26,27] and the small peak at 287.7 eV is typical for more oxidized carbon groups on an anodized carbon surface.[S26,28] No other peaks are evident in this region.

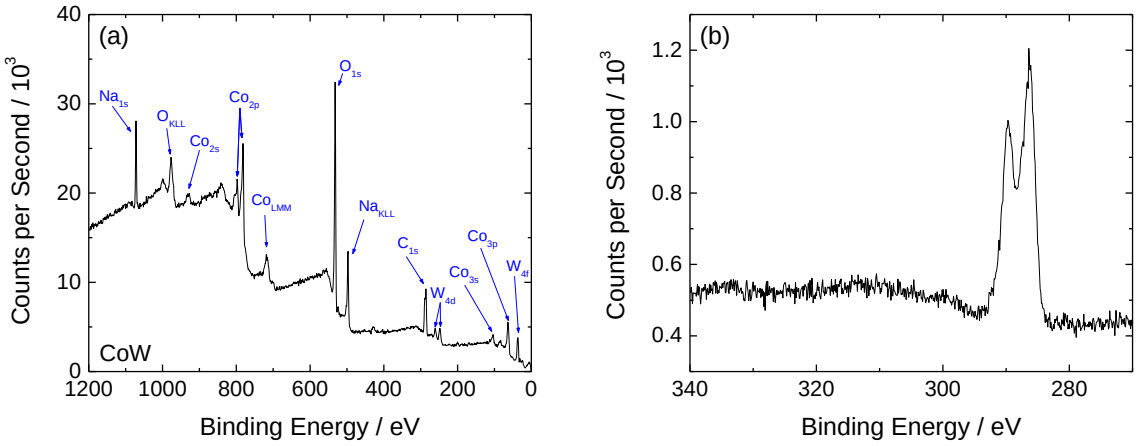

Figure S24. XPS of electrodeposited CoW on glassy carbon. (a) XPS survey scans with XPS and Auger peaks assigned as labeled. Note that the presence of Na is likely due to adsorbed ions from the deposition bath. (b) High resolution scans of the Ir4d/Pt4d/Ru3d region. The peak at 284.3 eV is the expected C1s peak for graphitic carbon in glassy carbon,[S26,27] and the peak at 287.7 eV is typical for more oxidized carbon groups on an anodized carbon surface.[S26,28] No other peaks are evident in this region.

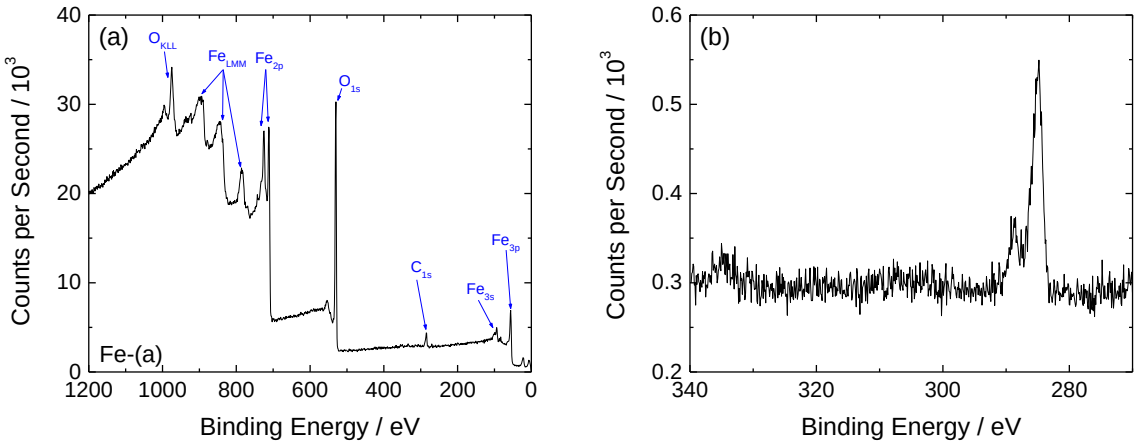

Figure S25. XPS of electrodeposited Fe-(a) on glassy carbon. (a) XPS survey scans with XPS and Auger peaks assigned as labeled. (b) High resolution scans of the Ir4d/Pt4d/Ru3d region. The peak at 284.3 eV is the expected C1s peak for graphitic carbon in glassy carbon,[S26,27] and the small peak at 287.7 eV is typical for more oxidized carbon groups on an anodized carbon surface.[S26,28] No other peaks are evident in this region.

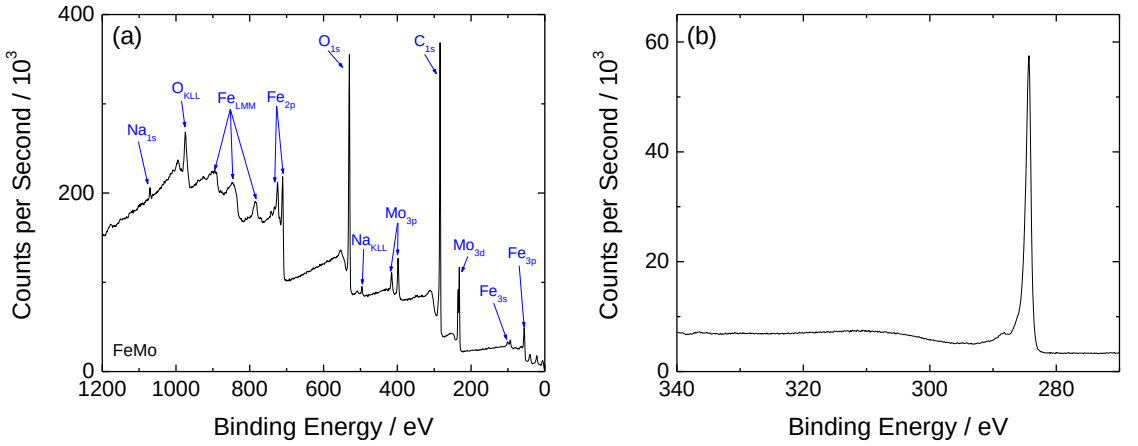

Figure S26. XPS of electrodeposited FeMo on glassy carbon. (a) XPS survey scans with XPS and Auger peaks assigned as labeled. Note that the presence of Na is likely due to adsorbed ions from the deposition bath. (b) High resolution scans of the Ir4d/Pt4d/Ru3d region. The peak at 284.3 eV is the expected C1s peak for graphitic carbon in glassy carbon,[S26,27] and the small shoulder at 287.7 eV is typical for more oxidized carbon groups on an anodized carbon surface.[S26,28] No other peaks are evident in this region.

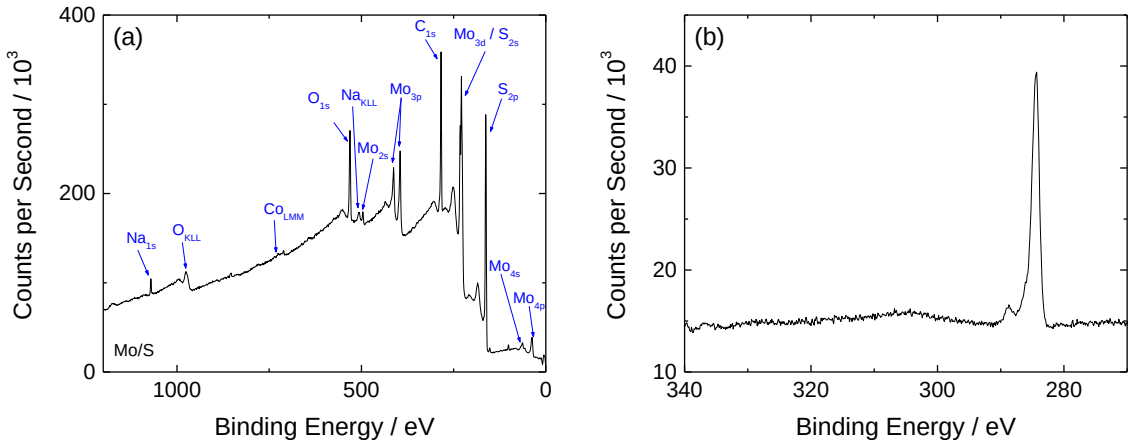

Figure S27. XPS of electrodeposited Mo/S on glassy carbon. (a) XPS survey scans with XPS and Auger peaks assigned as labeled. Small peaks barely above baseline at 99 eV and 149 eV are assigned to Si 2p and Si 2s, respectively. Note that the presence of Na is likely due to adsorbed ions from the deposition bath, and the presence of Si is likely due to residual SiC from the pre-electrolysis polishing. (b) High resolution scans of the Ir4d/Pt4d/Ru3d region. The peak at 284.3 eV is the expected C1s peak for graphitic carbon in glassy carbon,[S26,27] and the small peak at 287.7 eV is typical for more oxidized carbon groups on an anodized carbon surface.[S26,28] No other peaks are evident in this region.

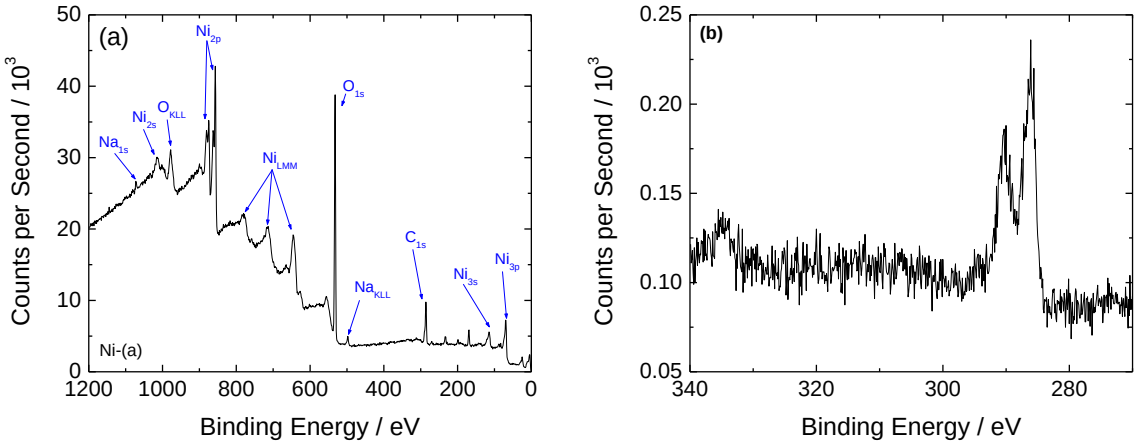

Figure S28. XPS of electrodeposited Ni-(a) on glassy carbon. (a) XPS survey scans with XPS and Auger peaks assigned as labeled. Small peaks at 169 eV and 232 eV are not labeled, but are assigned as S_{2s} and S_{2p} peaks, respectively. Note that the presence of S is likely due to adsorbed ions from the deposition bath. (b) High resolution scans of the Ir4d/Pt4d/Ru3d region. The peak at 284.3 eV is the expected C1s peak for graphitic carbon in glassy carbon,[S26,27] and the peak at 287.7 eV is typical for more oxidized carbon groups on an anodized carbon surface.[S26,28] No other peaks are evident in this region.

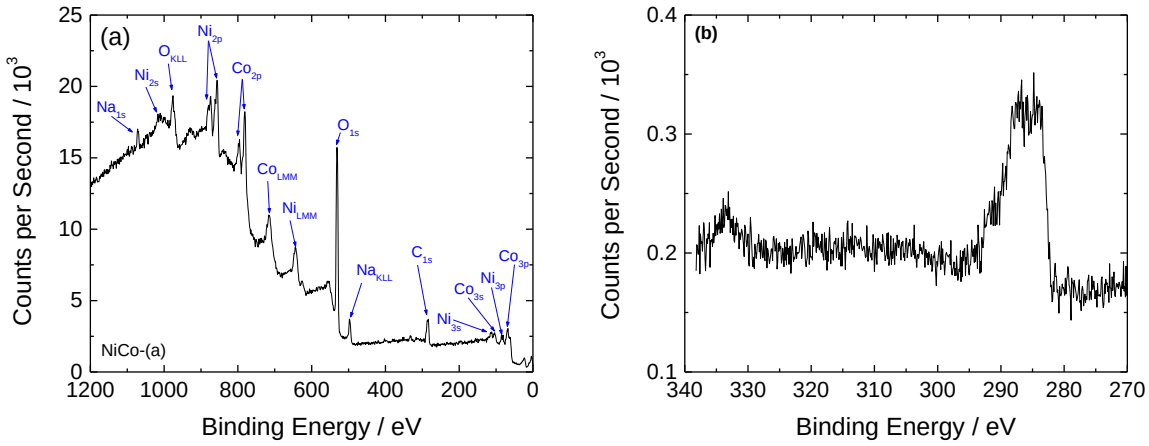

Figure S29. XPS of electrodeposited NiCo-(a) on glassy carbon. (a) XPS survey scans with XPS and Auger peaks assigned as labeled. Note that the presence of Na is likely due to adsorbed ions from the deposition bath. (b) High resolution scans of the Ir4d/Pt4d/Ru3d region. The broad peak at 286 eV is attributed to the convolution of two peaks: a peak at 284.3 eV expected C1s peak for graphitic carbon in glassy carbon,[S26,27] and a peak at 287.7 eV typical for more oxidized carbon groups on an anodized carbon surface.[S26,28]

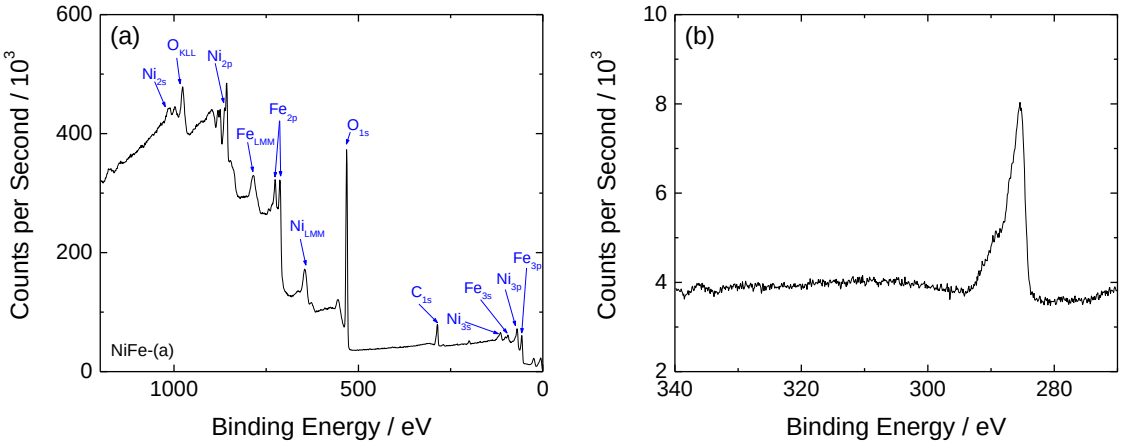

Figure S30. XPS of electrodeposited NiFe-(a) on glassy carbon. (a) XPS survey scans with XPS and Auger peaks assigned as labeled. The small peak barely above baseline at 197 eV is not labeled, but is assigned as Cl 2p. Note that the presence of Cl is likely due to adsorbed ions from the deposition bath. (b) High resolution scans of the Ir4d/Pt4d/Ru3d region. The peak at 284.3 eV is the expected C1s peak for graphitic carbon in glassy carbon,[S26,27] and the shoulder at 287.7 eV is typical for more oxidized carbon groups on an anodized carbon surface.[S26,28] No other peaks are evident in this region.

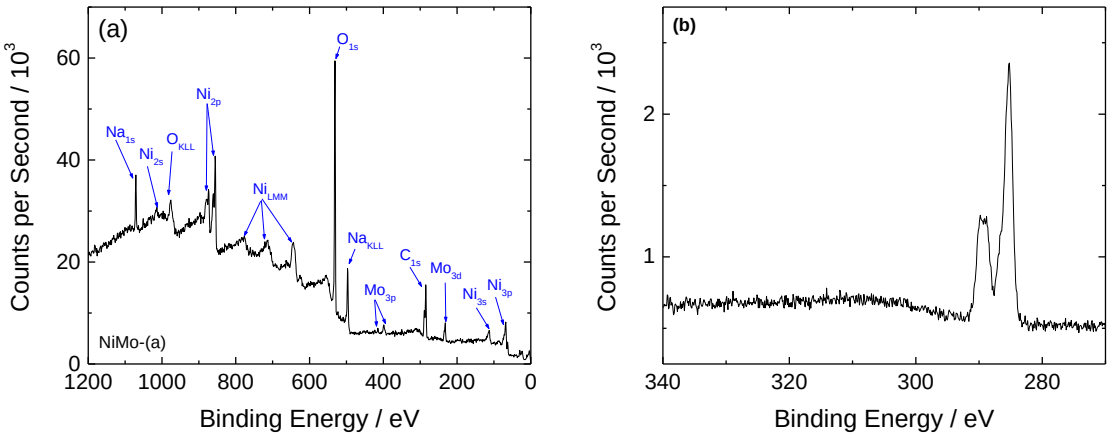

Figure S31. XPS of electrodeposited NiMo-(a) on glassy carbon. (a) XPS survey scans with XPS and Auger peaks assigned as labeled. Note that the presence of Na is likely due to adsorbed ions from the deposition bath. (b) High resolution scans of the Ir4d/Pt4d/Ru3d region. The peak at 284.3 eV is the expected C_{1s} peak for graphitic carbon in glassy carbon,[S26,27] and the peak at 287.7 eV is typical for more oxidized carbon groups on an anodized carbon surface.[S26,28] No other peaks are evident in this region.

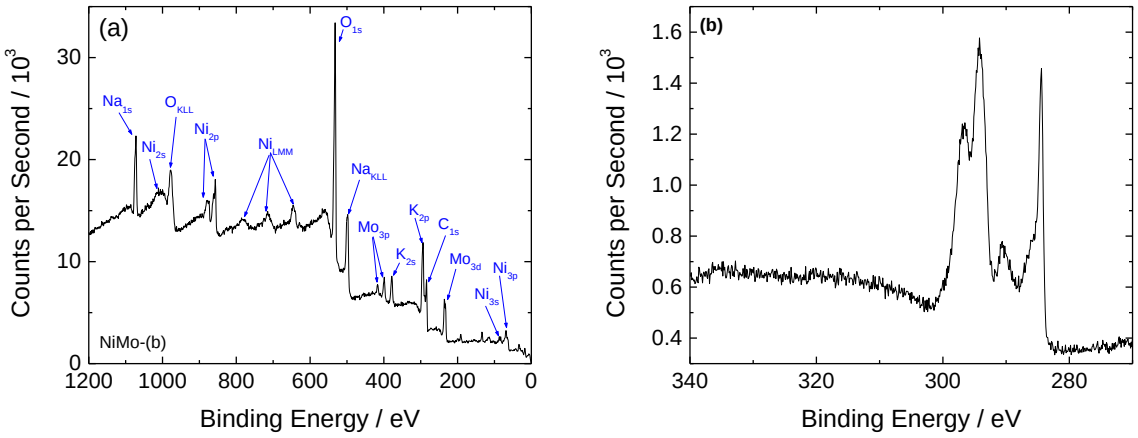

Figure S32. XPS of electrodeposited NiMo-(b) on glassy carbon. (a) XPS survey scans with XPS and Auger peaks assigned as labeled. The small peaks at 135 eV and 191 eV are not labeled, but are assigned as P_{2p} and P_{2s} peaks, respectively. Note that the presence of Na, K, and P is likely due to adsorbed ions from the deposition bath. (b) High resolution scans of the Ir4d/Pt4d/Ru3d region. The peak at 284.3 eV is the expected C_{1s} peak for graphitic carbon in glassy carbon.[S26,27] The peak at 290.2 eV is typical for carbonate species,[S29,30] presumably adsorbed onto the surface from the deposition bath. The peaks at 294.1 eV and 296.6 eV are assigned to the K_{2p} peaks. No other peaks are evident in this region.

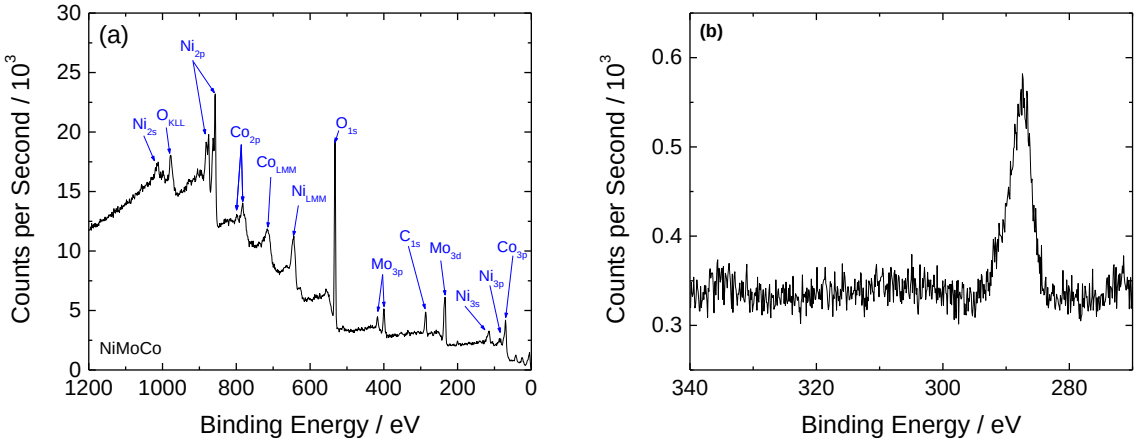

Figure S33. XPS of electrodeposited NiMoCo on glassy carbon. (a) XPS survey scans with XPS and Auger peaks assigned as labeled. (b) High resolution scans of the $Ir_{4d}/Pt_{4d}/Ru_{3d}$ region. The peak at 287.7 eV typical for oxidized carbon groups on an anodized carbon surface.[S26,28] No other peaks are evident in this region.

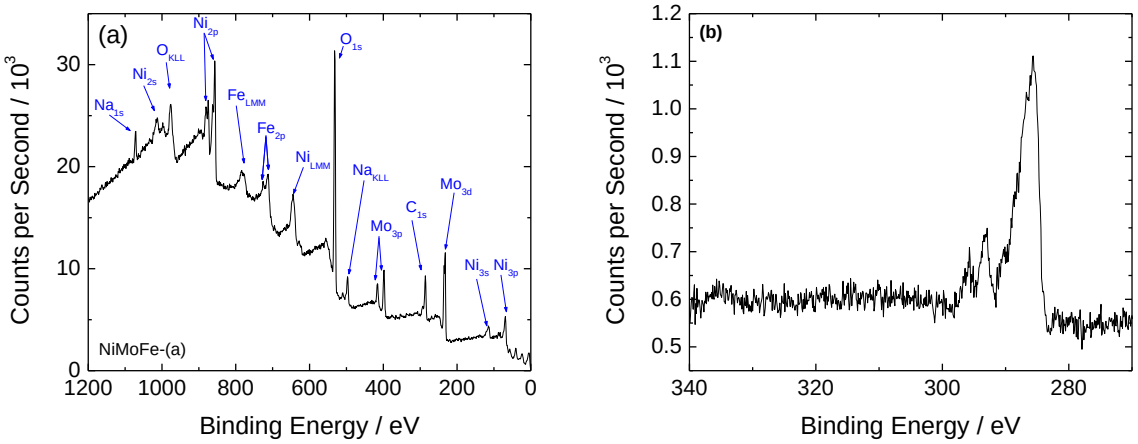

Figure S34. XPS of electrodeposited NiMoFe-(a) on glassy carbon. (a) XPS survey scans with XPS and Auger peaks assigned as labeled. Note that the presence of Na is likely due to adsorbed ions from the deposition bath. (b) High resolution scans of the $Ir_{4d}/Pt_{4d}/Ru_{3d}$ region. The peak at 284.3 eV is the expected C_{1s} peak for graphitic carbon in glassy carbon.[S26,27] The peaks at 294.1 eV and 296.6 eV are assigned to the K_{2p} peaks, presumably adsorbed onto the surface from the deposition bath. No other peaks are evident in this region.

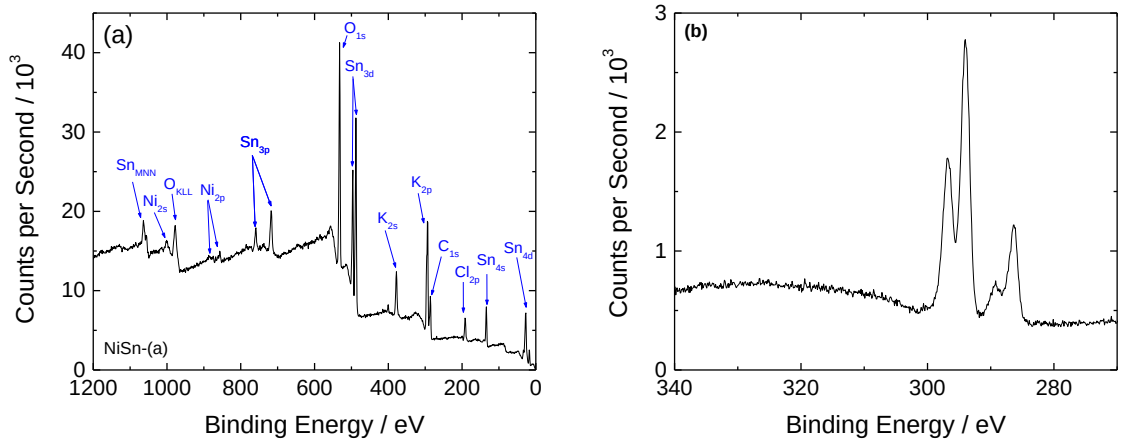

Figure S35. XPS of electrodeposited NiSn-(a) on glassy carbon. (a) XPS survey scans with XPS and Auger peaks assigned as labeled. Note that the presence of K and Cl are likely due to adsorbed ions from the deposition bath. (b) High resolution scans of the $Ir_{4d}/Pt_{4d}/Ru_{3d}$ region. The peak at 284.3 eV is the expected C_{1s} peak for graphitic carbon in glassy carbon,[S26,27] and the small peak at 287.7 eV is typical for more oxidized carbon groups on an anodized carbon surface.[S26,28] The peaks at 294.1 eV and 296.6 eV are assigned to the K_{2p} peaks. No other peaks are evident in this region.

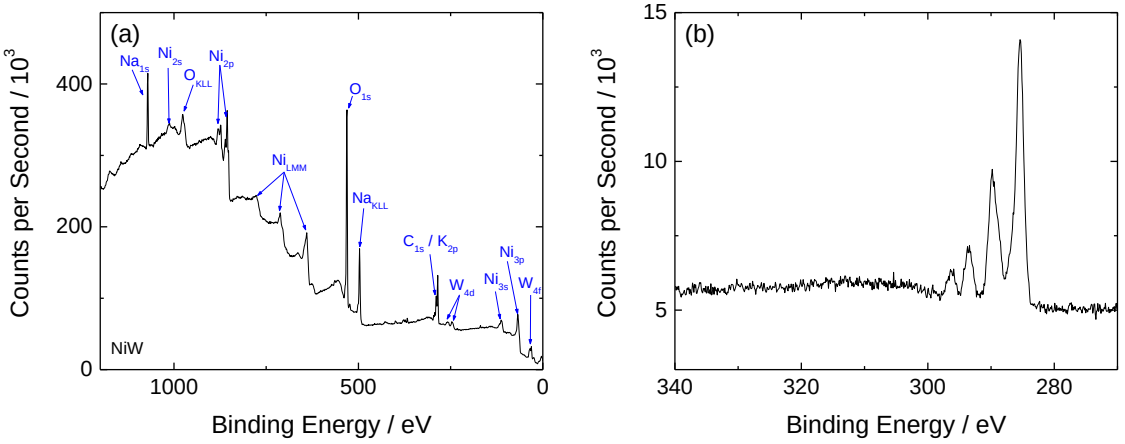

Figure S36. XPS of electrodeposited NiW on glassy carbon. (a) XPS survey scans with XPS and Auger peaks assigned as labeled. Note that the presence of Na and K is likely due to adsorbed ions from the deposition bath. (b) High resolution scans of the $Ir_{4d}/Pt_{4d}/Ru_{3d}$ region. The peak at 284.3 eV is the expected C_{1s} peak for graphitic carbon in glassy carbon.[S26,27] The peak at 290.2 eV is typical for carbonate species,[S29,30] presumably adsorbed onto the surface from the deposition bath. The peaks at 294.1 eV and 296.6 eV are assigned to the K_{2p} peaks. No other peaks are evident in this region.

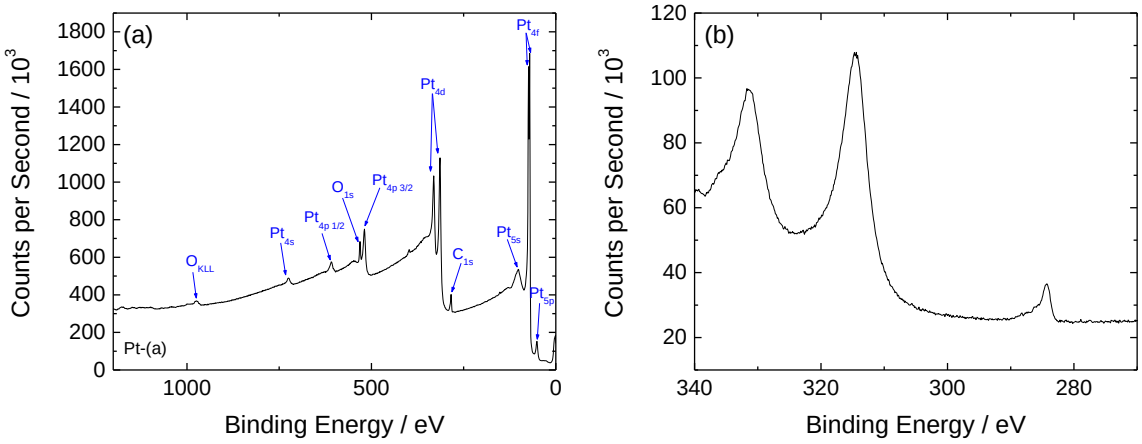

Figure S37. XPS of a Pt-(a) electrode. (a) XPS survey scans with XPS and Auger peaks assigned as labeled. (b) High resolution scans of the $Ir_{4d}/Pt_{4d}/Ru_{3d}$ region. The peak at 284.3 eV is the expected C_{1s} peak for graphitic carbon.[S26,27] The peaks at 314.6 and 331.4 eV are assigned to Pt_{4d} peaks.

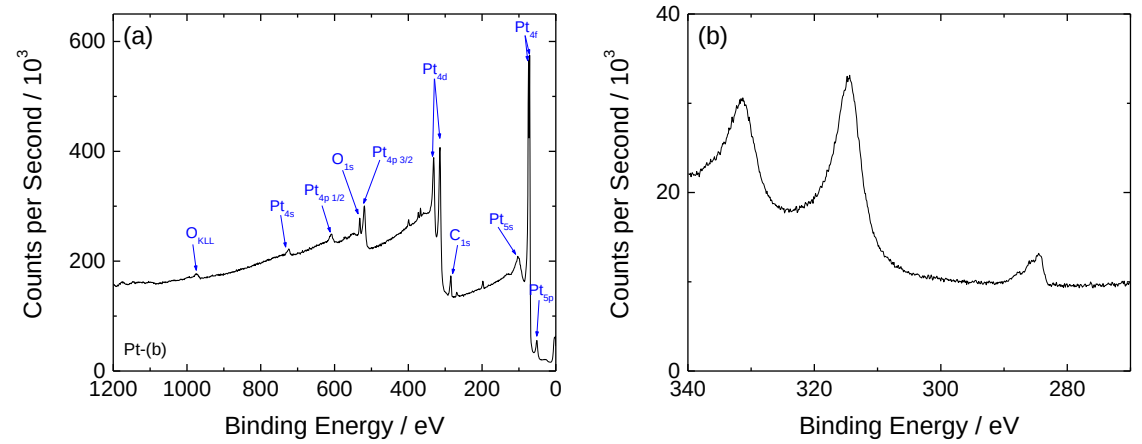

Figure S38. XPS of a Pt-(b) electrode. (a) XPS survey scans with XPS and Auger peaks assigned as labeled. The small peaks barely above baseline at 197 eV and 269 eV are not labeled, but are assigned as Cl 2p and Cl 2s peaks, respectively. Note that the presence of Cl is likely due to adsorbed ions from the deposition bath. (b) High resolution scans of the $Ir_{4d}/Pt_{4d}/Ru_{3d}$ region. The peak at 284.3 eV is the expected C_{1s} peak for graphitic carbon.[S26,27] The peaks at 314.6 and 331.4 eV are assigned to Pt_{4d} peaks.

Section S10: XPS of OER Materials (as-deposited)†

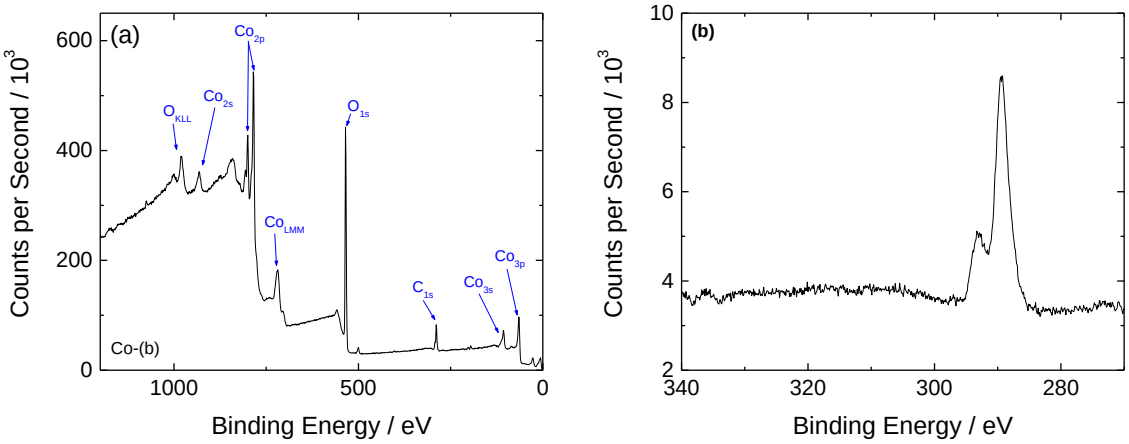

Figure S39. XPS of electrodeposited Co-(b) on glassy carbon. (a) XPS survey scans with XPS and Auger peaks assigned as labeled. The small peaks barely above baseline at 506 eV and 1070 eV are not labeled, but are assigned as the Na_{KLL} Auger transition peak and the Na_{1s} peak, respectively. Note that the presence of Na is likely due to adsorbed ions from the deposition bath. (b) High resolution scans of the Ir4d/Pt4d/Ru3d region. The peak at 284.3 eV is the expected C1s peak for graphitic carbon in glassy carbon,[S26,27] and the small peak at 287.7 eV is typical for more oxidized carbon groups on an anodized carbon surface.[S26,28] No other peaks are evident in this region.

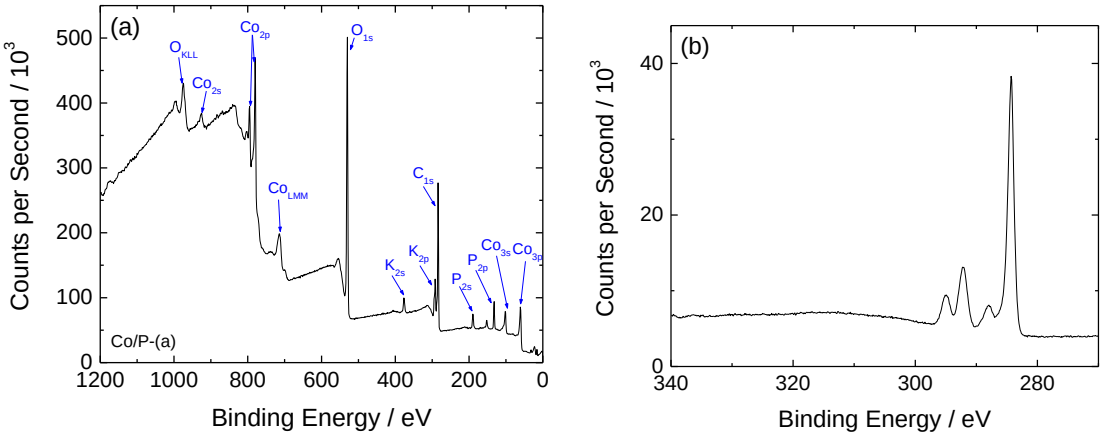

Figure S40. XPS of electrodeposited Co/P-(a) on glassy carbon. (a) XPS survey scans with XPS and Auger peaks assigned as labeled. The small peaks barely above baseline at 149 eV is assigned to Si 2s (the expected Si 2p peak at 99 eV likely overlaps with that of Co 3s). Note that the presence of K is likely due to adsorbed ions from the deposition bath, and the presence of Si is likely due to residual SiC from the pre-electrolysis polishing. (b) High resolution scans of the Ir4d/Pt4d/Ru3d region. The peak at 284.3 eV is the expected C1s peak for graphitic carbon in glassy carbon,[S26,27] and the small peak at 287.7 eV is typical for more oxidized carbon groups on an anodized carbon surface.[S26,28] The peaks at 294.1 eV and 296.6 eV are assigned to the K_{2p} peaks. No other peaks are evident in this region.

†Note that the elemental composition of $NiCeCoO_x$-(a) ($Ni_{0.5}Fe_{0.3}Co_{0.17}Ce_{0.03}O_x$) and $NiCeCoO_x$-(b) ($Ni_{0.3}Fe_{0.07}Co_{0.2}Ce_{0.43}O_x$) was previously characterized using EDX and XPS and showed no evidence of noble-metal contamination.[S32] Representative XPS spectra are not shown here for those two materials.

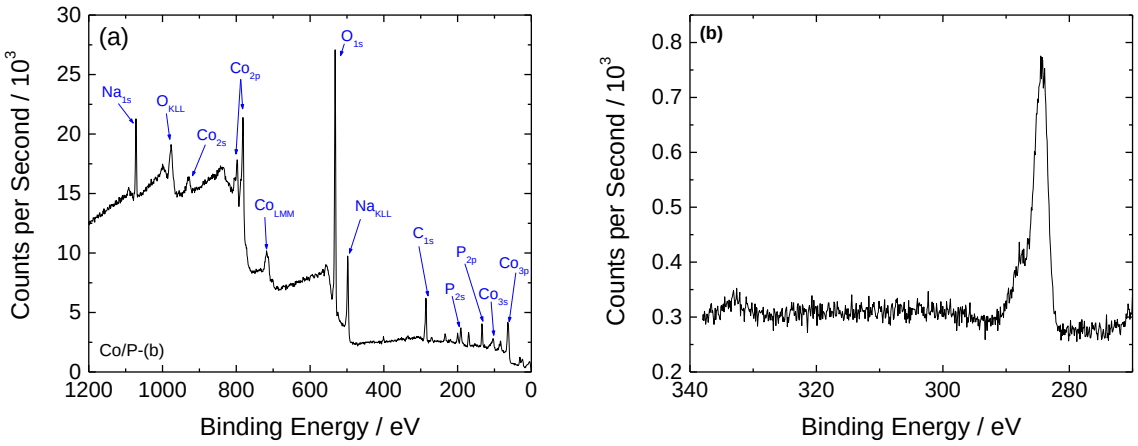

Figure S41. XPS of electrodeposited Co/P-(b) on glassy carbon. (a) XPS survey scans with XPS and Auger peaks assigned as labeled. Note that the presence of Na is likely due to adsorbed ions from the deposition bath. (b) High resolution scans of the Ir4d/Pt4d/Ru3d region. The peak at 284.3 eV is the expected C1s peak for graphitic carbon in glassy carbon,[S26,27] and the shoulder at 287.7 eV is typical for more oxidized carbon groups on an anodized carbon surface.[S26,28]

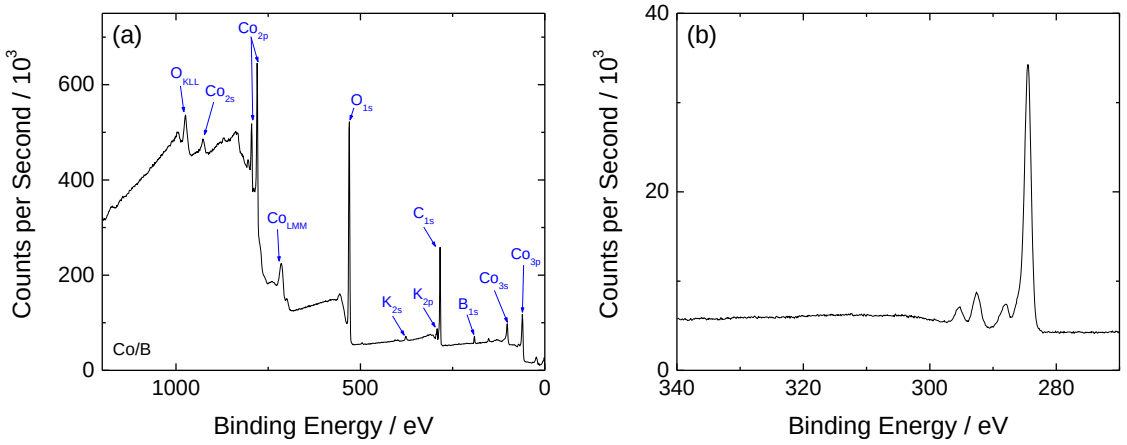

Figure S42. XPS of electrodeposited Co/B on glassy carbon. (a) XPS survey scans with XPS and Auger peaks assigned as labeled. Note that the presence of K is likely due to adsorbed ions from the deposition bath. (b) High resolution scans of the Ir4d/Pt4d/Ru3d region. The peak at 284.3 eV is the expected C1s peak for graphitic carbon in glassy carbon,[S26,27] and the small peak at 287.7 eV is typical for more oxidized carbon groups on an anodized carbon surface.[S26,28] The peaks at 294.1 eV and 296.6 eV are assigned to the K_{2p} peaks. No other peaks are evident in this region.

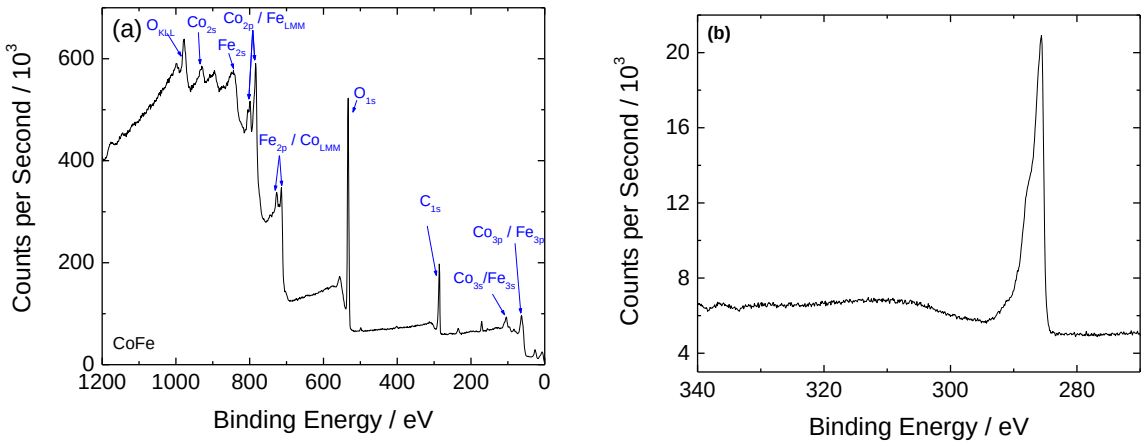

Figure S43. XPS of electrodeposited CoFe on glassy carbon. (a) XPS survey scans with XPS and Auger peaks assigned as labeled. The significant overlap between expected Co and Fe peaks prevents unambiguous assignment. Small peaks at 169 eV and 232 eV are not labeled, but are assigned as S_{2s} and S_{2p} peaks, respectively. Note that the presence of S is likely due to adsorbed ions from the deposition bath. (b) High resolution scans of the $Ir_{4d}/Pt_{4d}/Ru_{3d}$ region. The peak at 284.3 eV is the expected C_{1s} peak for graphitic carbon in glassy carbon,[S26,27] and the shoulder at 287.7 eV is typical for more oxidized carbon groups on an anodized carbon surface.[S26,28] No other peaks are evident in this region.

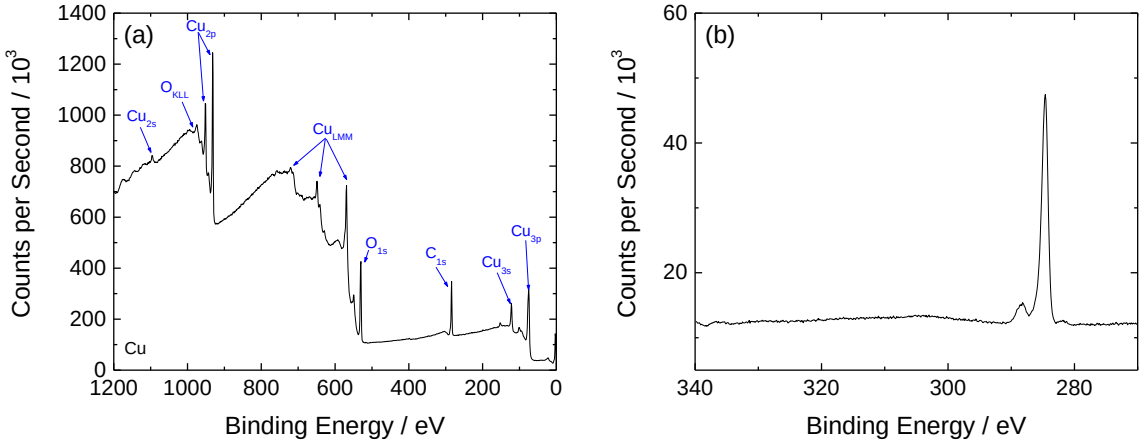

Figure S44. XPS of electrodeposited Cu on glassy carbon. (a) XPS survey scans with XPS and Auger peaks assigned as labeled. (b) High resolution scans of the $Ir_{4d}/Pt_{4d}/Ru_{3d}$ region. The peak at 284.3 eV is the expected C_{1s} peak for graphitic carbon in glassy carbon,[S26,27] and the small peak at 287.7 eV is typical for more oxidized carbon groups on an anodized carbon surface.[S26,28] No other peaks are evident in this region.

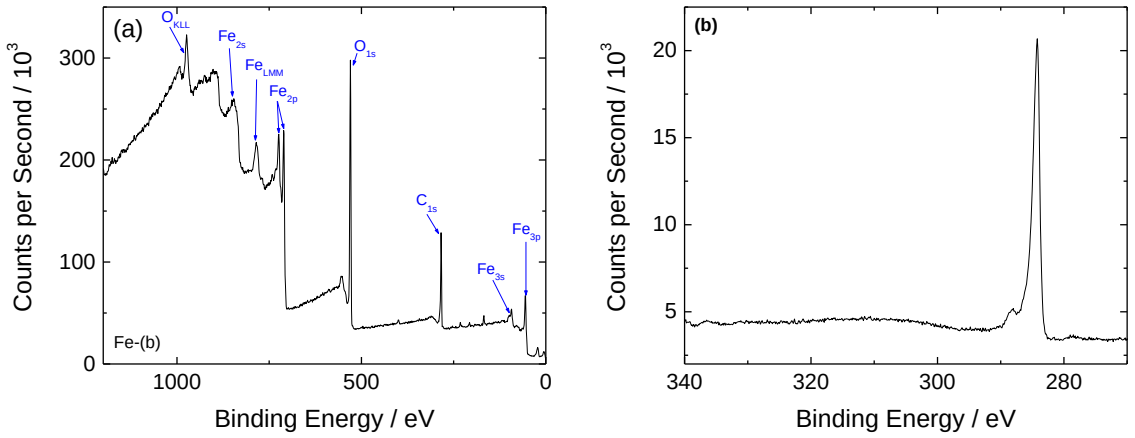

Figure S45. XPS of electrodeposited Fe-(b) on glassy carbon. (a) XPS survey scans with XPS and Auger peaks assigned as labeled. Small peaks at 169 eV and 232 eV are not labeled, but are assigned as S_{2s} and S_{2p} peaks, respectively. Note that the presence of S is likely due to adsorbed ions from the deposition bath. (b) High resolution scans of the $Ir_{4d}/Pt_{4d}/Ru_{3d}$ region. The peak at 284.3 eV is the expected C_{1s} peak for graphitic carbon in glassy carbon,[S26,27] and the shoulder at 287.7 eV is typical for more oxidized carbon groups on an anodized carbon surface.[S26,28] No other peaks are evident in this region.

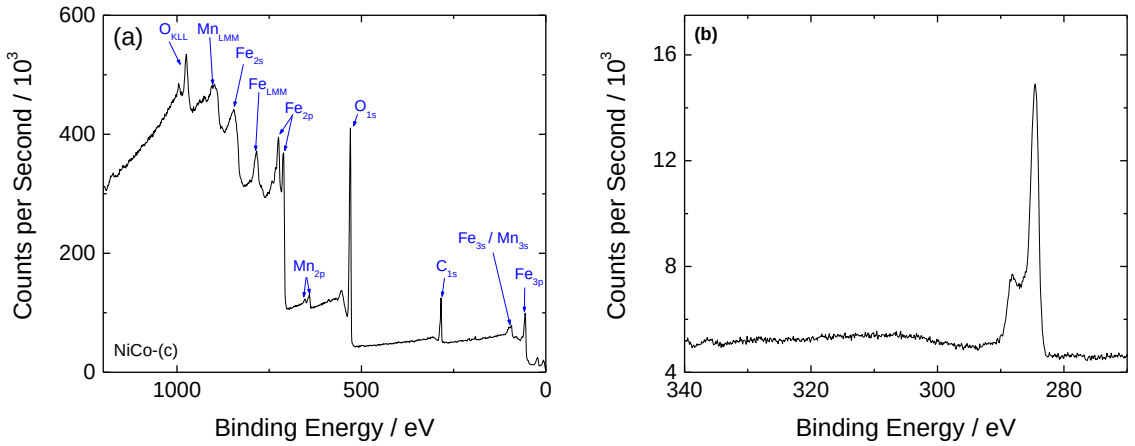

Figure S46. XPS of electrodeposited FeMn on glassy carbon. (a) XPS survey scans with XPS and Auger peaks assigned as labeled. (b) High resolution scans of the $Ir_{4d}/Pt_{4d}/Ru_{3d}$ region. The peak at 284.3 eV is the expected C_{1s} peak for graphitic carbon in glassy carbon,[S26,27] and the shoulder at 287.7 eV is typical for more oxidized carbon groups on an anodized carbon surface.[S26,28] No other peaks are evident in this region.

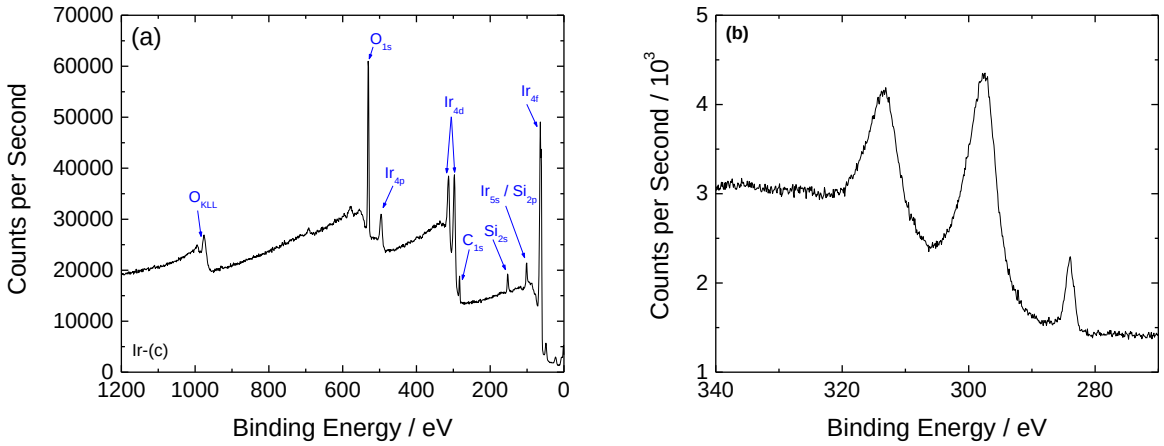

Figure S47. XPS of sputtered Ir electrode on glassy carbon. (a) XPS survey scans with XPS and Auger peaks assigned as labeled. Note that the presence of Si is likely due to Si contamination from the reactive sputtering preparation. (b) High resolution scans of the $Ir_{4d}/Pt_{4d}/Ru_{3d}$ region. The peak at 284.3 eV expected C_{1s} peak for graphitic carbon in glassy carbon.[S26,27] The peaks at 297.4 and 312.3 are assigned to the Ir_{4d} peaks.

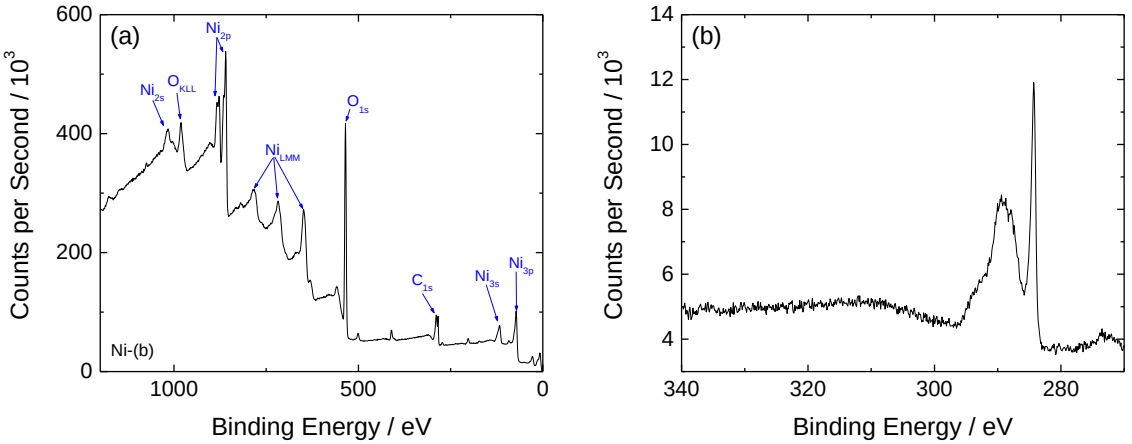

Figure S48. XPS of electrodeposited Ni-(b) electrode on glassy carbon. (a) XPS survey scans with XPS and Auger peaks assigned as labeled. (b) High resolution scans of the $Ir_{4d}/Pt_{4d}/Ru_{3d}$ region. The peak at 284.3 eV is the expected C_{1s} peak for graphitic carbon in glassy carbon.[S26,27] The broad peak at 290 eV is likely a convolution of peaks at 287.7 eV[S26,27] and 290.2 eV[S29,30] typical for more oxidized carbon species. No other peaks are evident in this region.

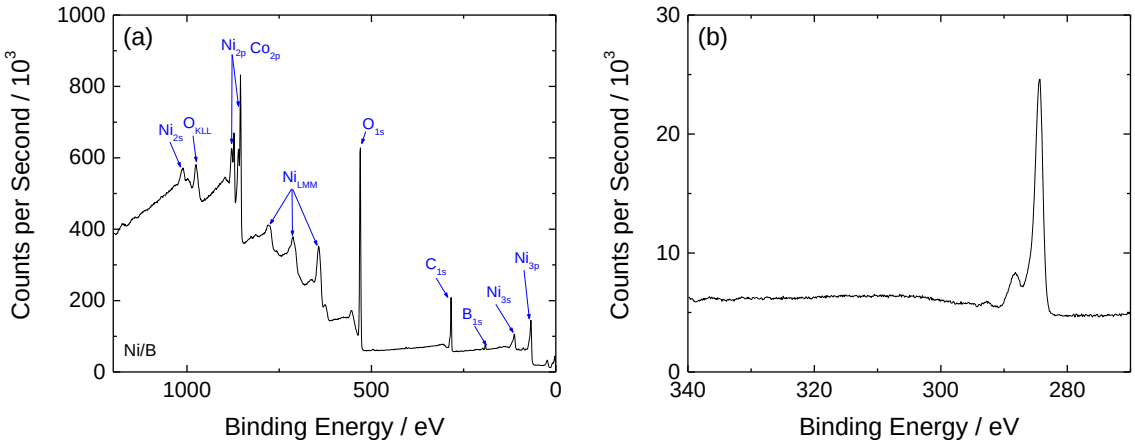

Figure S49. XPS of electrodeposited Ni/B on glassy carbon. (a) XPS survey scans with XPS and Auger peaks assigned as labeled. (b) High resolution scans of the Ir4d/Pt4d/Ru3d region. The peak at 284.3 eV is the expected C1s peak for graphitic carbon in glassy carbon,[S26,27] and the shoulder at 287.7 eV is typical for more oxidized carbon groups on an anodized carbon surface.[S26,28] No other peaks are evident in this region.

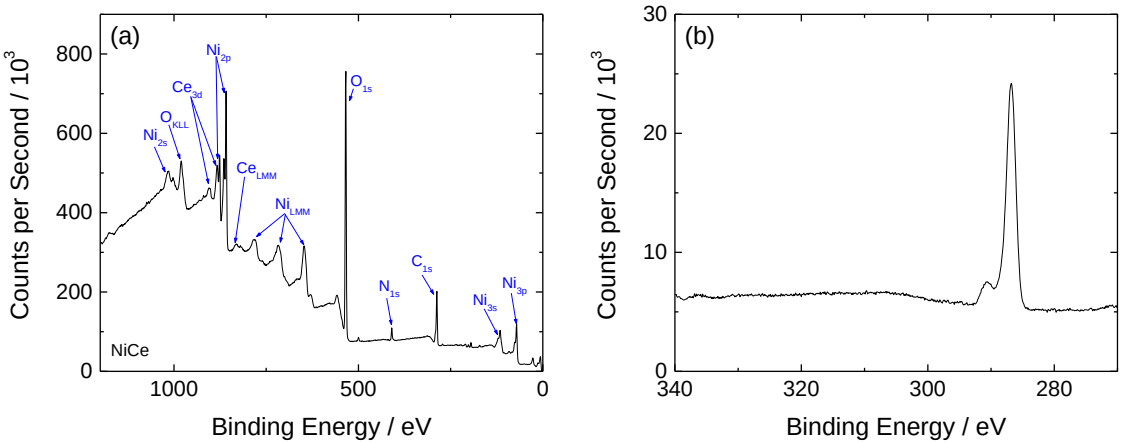

Figure S50. XPS of electrodeposited NiCe on glassy carbon. (a) XPS survey scans with XPS and Auger peaks assigned as labeled. (b) High resolution scans of the Ir4d/Pt4d/Ru3d region. The peak at 284.3 eV is the expected C1s peak for graphitic carbon in glassy carbon,[S26,27] and the shoulder at 287.7 eV is typical for more oxidized carbon groups on an anodized carbon surface.[S26,28] No other peaks are evident in this region.

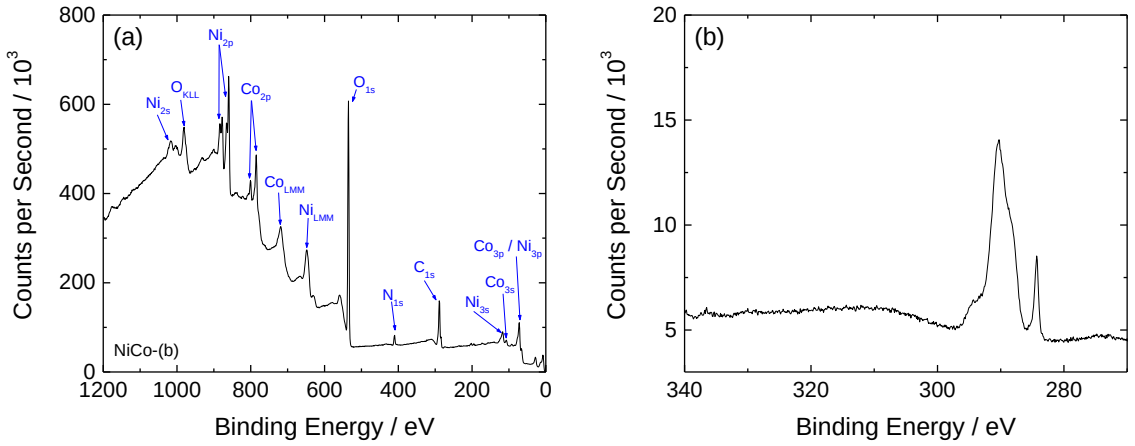

Figure S51. XPS of electrodeposited NiCo-(b) on glassy carbon. (a) XPS survey scans with XPS and Auger peaks assigned as labeled. (b) High resolution scans of the $Ir_{4d}/Pt_{4d}/Ru_{3d}$ region. The peak at 284.3 eV is the expected C_{1s} peak for graphitic carbon in glassy carbon.[S26,27] The broad peak at 290 eV is likely a convolution of peaks at 287.7 eV[S26,27] and 290.2 eV[S29,30] typical for more oxidized carbon species. No other peaks are evident in this region.

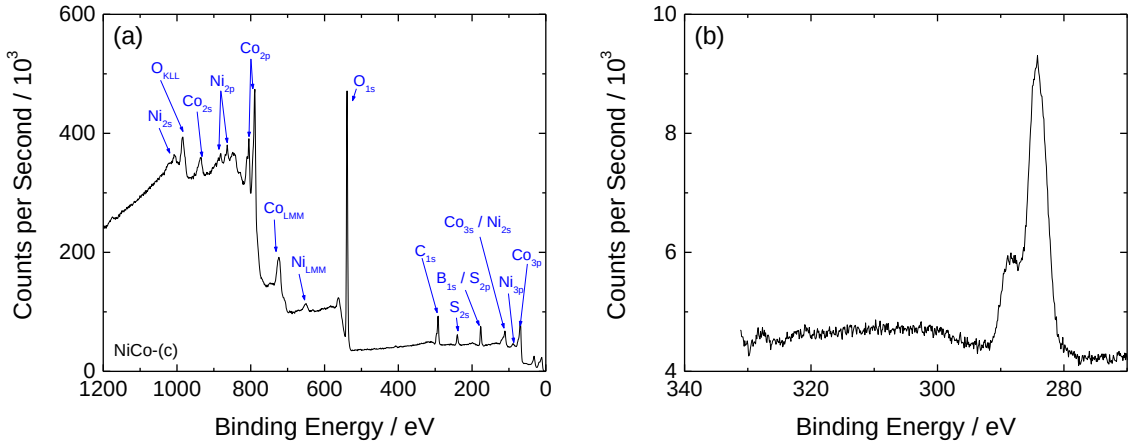

Figure S52. XPS of electrodeposited NiCo-(c) on glassy carbon. (a) XPS survey scans with XPS and Auger peaks assigned as labeled. Overlap between B_{1s} and S_{2p} peaks prevents unambiguous assignment. Note that the presence of S and possibly B is likely due to adsorbed ions from the deposition bath. (b) High resolution scans of the $Ir_{4d}/Pt_{4d}/Ru_{3d}$ region. The peak at 284.3 eV is the expected C_{1s} peak for graphitic carbon in glassy carbon,[S26,27] and the shoulder at 287.7 eV is typical for more oxidized carbon groups on an anodized carbon surface.[S26,28] No other peaks are evident in this region.

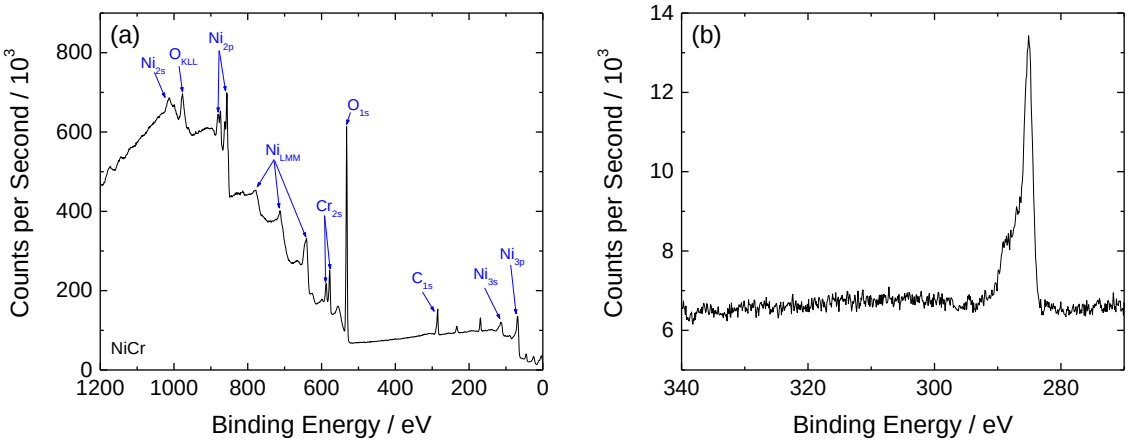

Figure S53. XPS of electrodeposited NiCr on glassy carbon. (a) XPS survey scans with XPS and Auger peaks assigned as labeled. Small peaks at 169 eV and 232 eV are not labeled, but are assigned as S_{2s} and S_{2p} peaks, respectively. Note that the presence of S is likely due to adsorbed ions from the deposition bath. (b) High resolution scans of the $Ir_{4d}/Pt_{4d}/Ru_{3d}$ region. The peak at 284.3 eV is the expected C_{1s} peak for graphitic carbon in glassy carbon,[S26,27] and the shoulder at 287.7 eV is typical for more oxidized carbon groups on an anodized carbon surface.[S26,28] No other peaks are evident in this region.

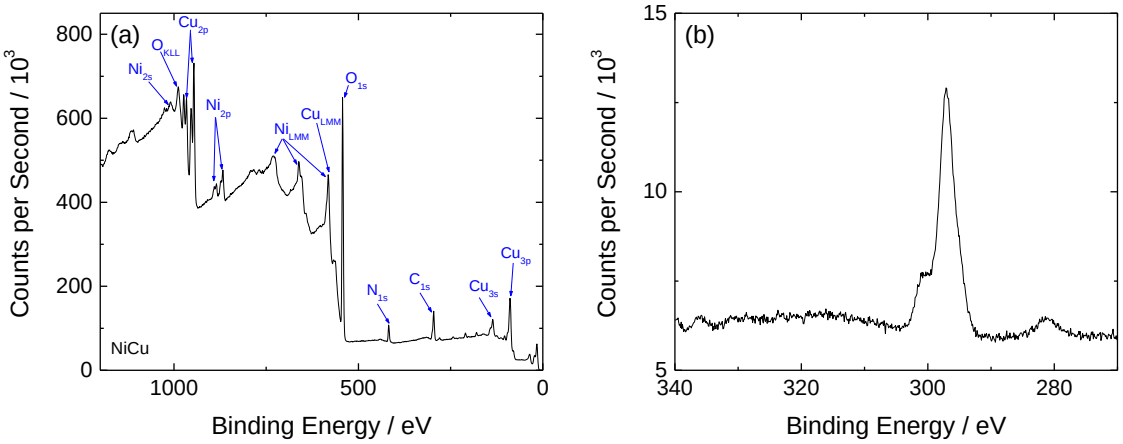

Figure S54. XPS of electrodeposited NiCu on glassy carbon. (a) XPS survey scans with XPS and Auger peaks assigned as labeled. (b) High resolution scans of the $Ir_{4d}/Pt_{4d}/Ru_{3d}$ region. The peak at 284.3 eV is the expected C_{1s} peak for graphitic carbon in glassy carbon,[S26,27] and the shoulder at 287.7 eV is typical for more oxidized carbon groups on an anodized carbon surface.[S26,28] No other peaks are evident in this region.

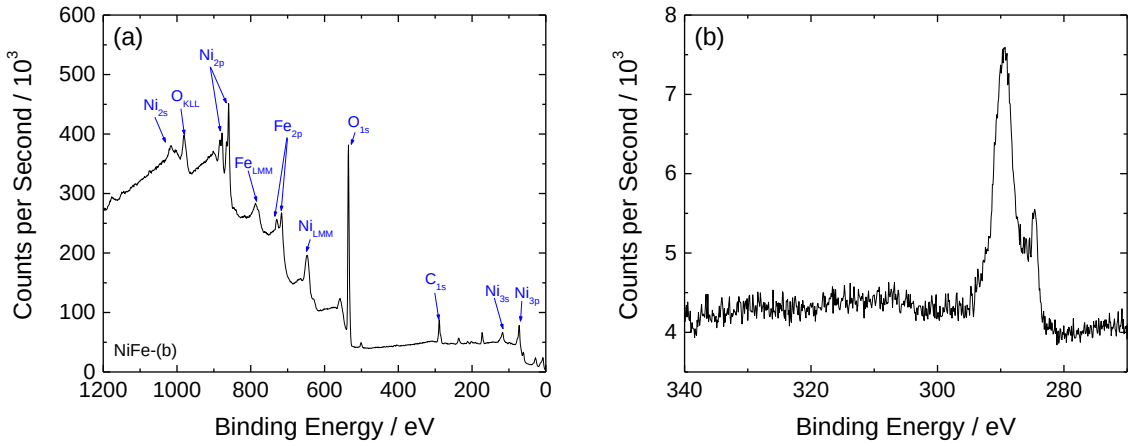

Figure S55. XPS of electrodeposited NiFe-(b) on glassy carbon. (a) XPS survey scans with XPS and Auger peaks assigned as labeled. Small peaks at 169 eV and 232 eV are not labeled, but are assigned as S_{2s} and S_{2p} peaks, respectively. Note that the presence of S is likely due to adsorbed ions from the deposition bath. (b) High resolution scans of the $Ir_{4d}/Pt_{4d}/Ru_{3d}$ region. The peak at 284.3 eV is the expected C_{1s} peak for graphitic carbon in glassy carbon.[S26,27] The broad peak at 290 eV is likely a convolution of peaks at 287.7 eV[S26,27] and 290.2 eV[S29,30] typical for more oxidized carbon species. No other peaks are evident in this region.

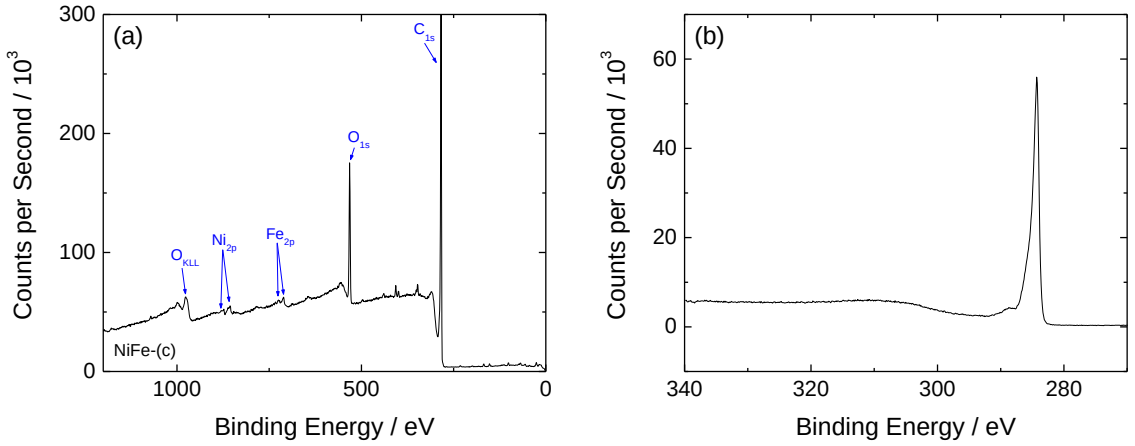

Figure S56. XPS of electrodeposited NiFe-(c) on glassy carbon. (a) XPS survey scans with XPS and Auger peaks assigned as labeled. (b) High resolution scans of the $Ir_{4d}/Pt_{4d}/Ru_{3d}$ region. The peak at 284.3 eV is the expected C_{1s} peak for graphitic carbon in glassy carbon,[S26,27] and the small shoulder at 287.7 eV is typical for more oxidized carbon groups on an anodized carbon surface.[S26,28]

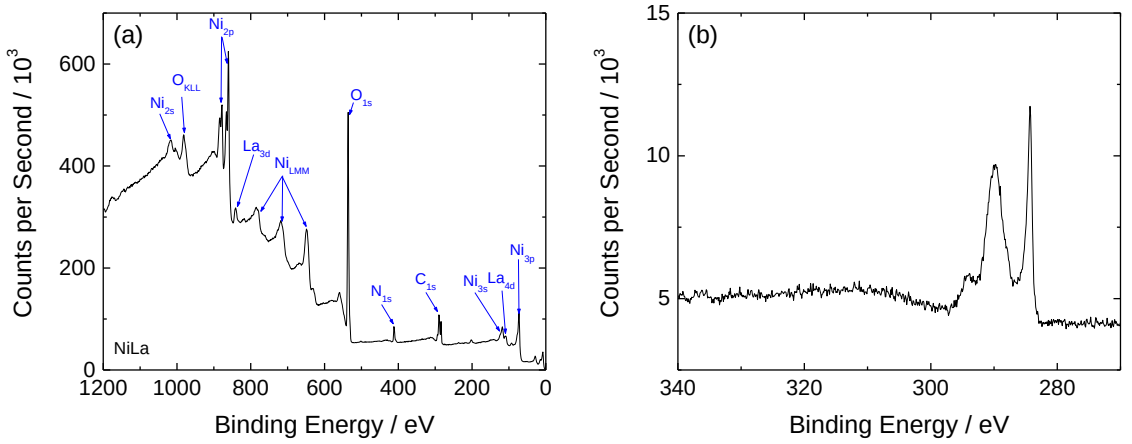

Figure S57. XPS of electrodeposited NiLa on glassy carbon. (a) XPS survey scans with XPS and Auger peaks assigned as labeled. Note that the presence of N is likely due to adsorbed ions from the deposition bath. (b) High resolution scans of the Ir4d/Pt4d/Ru3d region. The peak at 284.3 eV is the expected C1s peak for graphitic carbon in glassy carbon.[S26,27] The broad peak at 290 eV is likely a convolution of peaks at 287.7 eV[S26,27] and 290.2 eV[S29,30] typical for more oxidized carbon species. No other peaks are evident in this region.

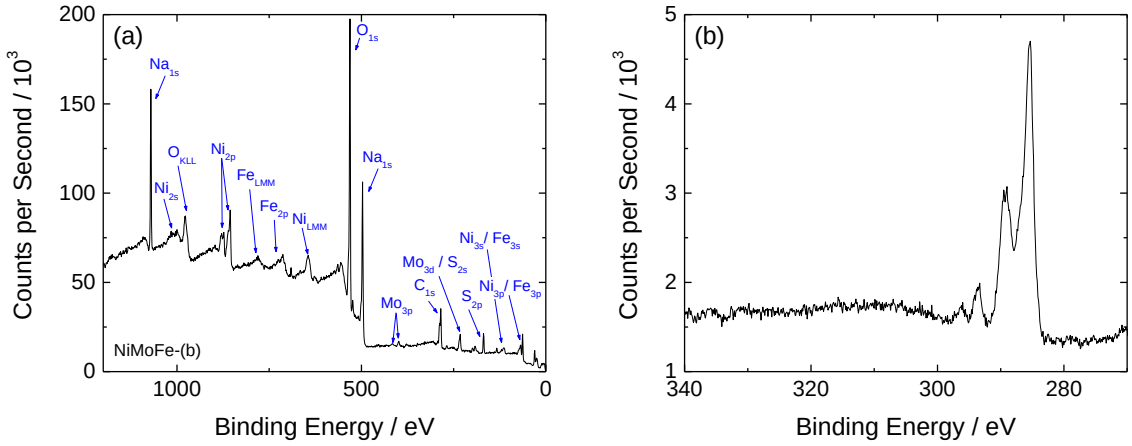

Figure S58. XPS of electrodeposited NiMoFe-(b) on glassy carbon. (a) XPS survey scans with XPS and Auger peaks assigned as labeled. Note that the presence of Na and S are likely due to adsorbed ions from the deposition bath. (b) High resolution scans of the Ir4d/Pt4d/Ru3d region. The peak at 284.3 eV is the expected C1s peak for graphitic carbon in glassy carbon,[S26,27] and the shoulder at 287.7 eV is typical for more oxidized carbon groups on an anodized carbon surface.[S26,28] The peaks at 294.1 eV and 296.6 eV are assigned to the K_{2p} peaks, presumably adsorbed onto the surface from the deposition bath.

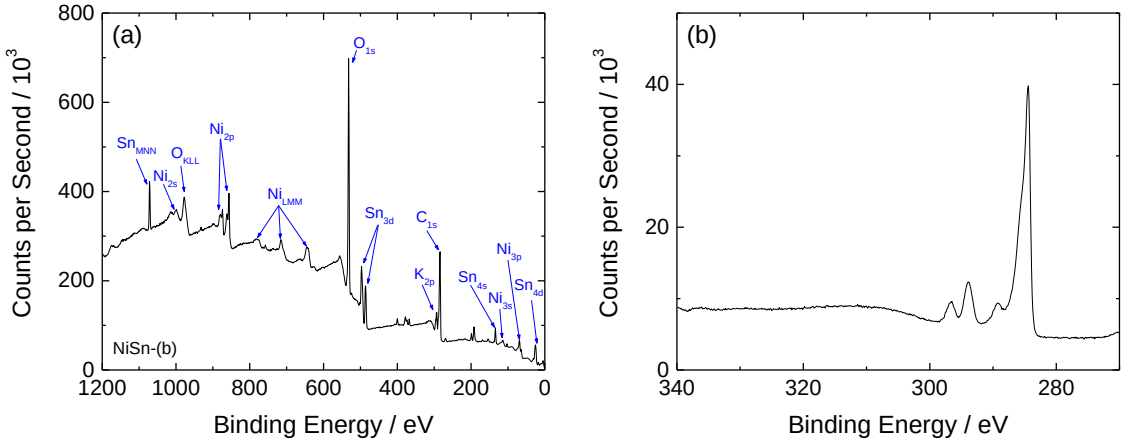

Figure S59. XPS of electrodeposited NiSn-(b) on glassy carbon. (a) XPS survey scans with XPS and Auger peaks assigned as labeled. The small peaks barely above baseline at 134 eV, 190 eV, 200 eV, 374 eV, and 399 eV are assigned to P 2p, P 2s, Cl 2p, K 2s, and N 1s, respectively. Note that the presence of K, P, Cl, and N is likely due to adsorbed ions from the deposition bath. (b) High resolution scans of the Ir4d/Pt4d/Ru3d region. The peak at 284.3 eV is the expected C1s peak for graphitic carbon in glassy carbon.[S26,27] The peaks at 294.1 eV and 296.6 eV are assigned to the K_{2p} peaks, presumably adsorbed onto the surface from the deposition bath. No other peaks are evident in this region.

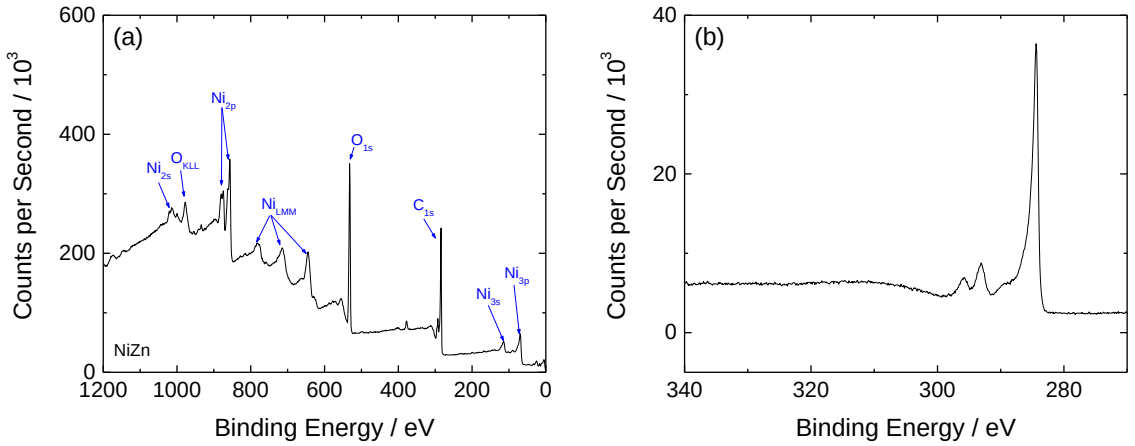

Figure S60. XPS of electrodeposited NiZn-(b) on glassy carbon. (a) XPS survey scans with XPS and Auger peaks assigned as labeled. The lack of Zn in the XPS spectra is likely due to Zn dissolution during the post-electrodeposition 24-h immersion in 28% KOH.[S24] The small peak at 374 eV is assigned to K 2s, and the presence of K is likely due to adsorbed ions from the post-electrodeposition KOH immersion bath. (b) High resolution scans of the Ir4d/Pt4d/Ru3d region. The peaks at 294.1 eV and 296.6 eV are assigned to the K_{2p} peaks, presumably adsorbed onto the surface from the post-electrodeposition KOH immersion bath. No other peaks are evident in this region.

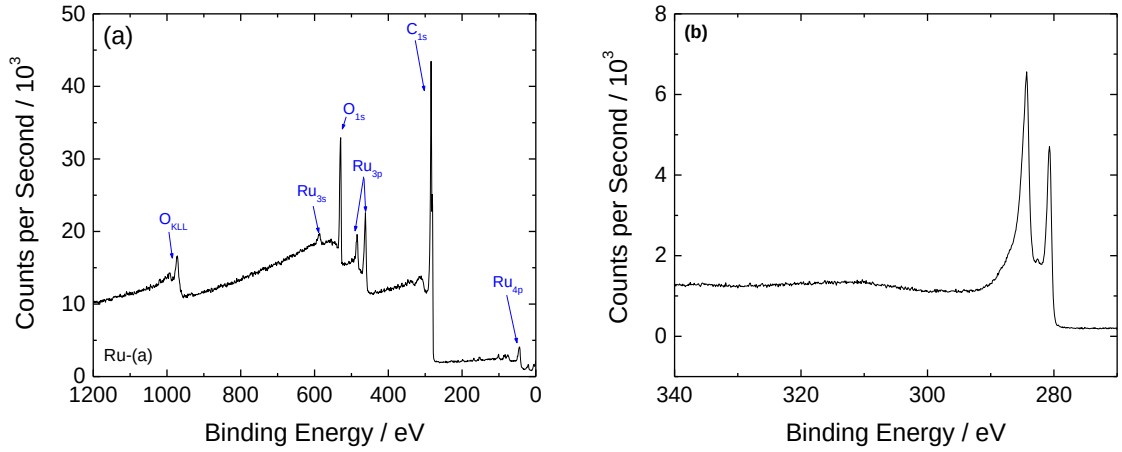

Figure S61. XPS of electrodeposited Ru-(a) on glassy carbon. (a) XPS survey scans with XPS and Auger peaks assigned as labeled. (b) High resolution scans of the Ir4d/Pt4d/Ru3d region. The peak at 284.3 eV is the expected C1s peak for graphitic carbon in glassy carbon.[S26,27] The peak at 280.7 is assigned to the Ru3d peak.

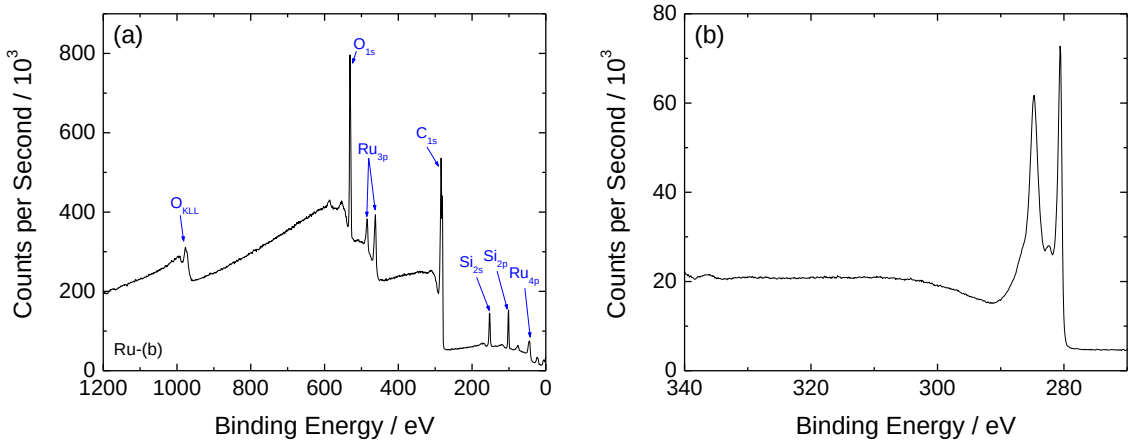

Figure S62. XPS of sputtered Ru-(b) on glassy carbon. XPS survey scans with XPS and Auger peaks assigned as labeled. Note that the presence of Si is likely due to Si contamination from the reactive sputtering preparation. (b) High resolution scans of the Ir4d/Pt4d/Ru3d region. The peak at 284.3 eV is the expected C1s peak for graphitic carbon in glassy carbon.[S26,27] The peak at 280.7 is assigned to the Ru3d peak.

Section S11: References

(S1) Savadogo, O.; Lavoie, H. *Int. J. Hydrogen Energy* **1992**, *17*, 473-477.
(S2) Fan, C.; Piron, D. L.; Sleb, A.; Paradis, P. *J. Electrochem. Soc.* **1994**, *141*, 382-387.
(S3) Jafarian, M.; Azizi, O.; Gobal, F.; Mahjani, M. G. *Int. J. Hydrogen Energy* **2007**, *32*, 1686-1693.
(S4) Solmaz, R.; Kardaş, G. *Electrochim. Acta* **2009**, *54*, 3726-3734.
(S5) Elezović, N. R.; Jović, V. D.; Krstajić, N. V. *Electrochim. Acta* **2005**, *50*, 5594-5601.
(S6) Merki, D.; Fierro, S.; Vrubel, H.; Hu, X. *Chem. Sci.* **2011**, *2*, 1262-1267.
(S7) Merki, D.; Vrubel, H.; Rovelli, L.; Fierro, S.; Hu, X. *Chem. Sci.* **2012**, *3*, 2515-2525.
(S8) Raj, I. A.; Vasu, K. I. *J. Appl. Electrochem.* **1990**, *20*, 32-38.
(S9) Navarro-Flores, E.; Chong, Z.; Omanovic, S. *J. Mol. Catal. A: Chem.* **2005**, *226*, 179-197.
(S10) Krstajić, N. V.; Jović, V. D.; Gajić-Krstajić, L.; Jović, B. M.; Antozzi, A. L.; Martelli, G. N. *Int. J. Hydrogen Energy* **2008**, *33*, 3676-3687.
(S11) Fan, C.; Piron, D. L.; Paradis, P. *Electrochim. Acta* **1994**, *39*, 2715-2722.
(S12) Raj, I. A.; Vasu, K. I. *J. Appl. Electrochem.* **1992**, *22*, 471-477.
(S13) Yamashita, H.; Yamamura, T.; Yoshimoto, K. *J. Electrochem. Soc.* **1993**, *140*, 2238-2243.
(S14) Merrill, M. D.; Dougherty, R. C. *J. Phys. Chem. C* **2008**, *112*, 3655-3666.
(S15) Surendranath, Y.; Dincă, M.; Nocera, D. G. *J. Am. Chem. Soc.* **2009**, *131*, 2615-2620.
(S16) Kanan, M. W.; Nocera, D. G. *Science* **2008**, *321*, 1072-1075.
(S17) Surówka, J.; Budniok, A.; Bzowski, B.; Warczewski, J. *Thin Solid Films* **1997**, *307*, 233-239.
(S18) Corrigan, D. A.; Bendert, R. M. *J. Electrochem. Soc.* **1989**, *136*, 723-728.
(S19) Dincă, M.; Surendranath, Y.; Nocera, D. G. *Proc. Natl. Acad. Sci.* **2010**, *107*, 10337-10341.
(S20) Ho, J. C. K.; Piron, D. L. *J. Appl. Electrochem.* **1996**, *26*, 515-521.
(S21) Li, X.; Walsh, F. C.; Pletcher, D. *Phys. Chem. Chem. Phys.* **2011**, *13*, 1162-1167.
(S22) Corrigan, D. A. *J. Electrochem. Soc.* **1987**, *134*, 377-384.
(S23) Jayalakshmi, M.; Kim, W. Y.; Jung, K. D.; Joo, O. S. *Int. J. Electrochem. Sci.* **2008**, *3*, 908.
(S24) Santos, M. B. F.; da Silva, E. P.; Andrade Jr, R.; Dias, J. A. F. *Electrochim. Acta* **1992**, *37*, 29-32.
(S25) Tsuji, E.; Imanishi, A.; Fukui, K.-i.; Nakato, Y. *Electrochim. Acta* **2011**, *56*, 2009-2016.
(S26) Cabaniss, G. E.; Diamantis, A. A.; Murphy, W. R.; Linton, R. W.; Meyer, T. J. *J. Am. Chem. Soc.* **1985**, *107*, 1845-1853.
(S27) McCreery, R. L. In *Electroanalytical Chemistry: A Series of Advances*; Bard, A. J., Ed.; Marcel Dekker: New York, 1991; Vol. 17, p 221-374.
(S28) Xie, Y.; Sherwood, P. M. A. *Chem. Mater.* **1991**, *3*, 164-168.
(S29) Gelius, U.; Hedén, P. F.; Hedman, J.; Lindberg, B. J.; Manne, R.; Nordberg, R.; Nordling, C.; Siegbahn, K. *Phys. Scr.* **1970**, *2*, 70.
(S30) Hammond, J. S.; Holubka, J. W.; deVries, J. E.; Dickie, R. A. *Corros. Sci.* **1981**, *21*, 239-253.